Conjugate solid-liquid phase change heat transfer in heatsink filled with phase change material-metal foam

Mohammad Ghalambaz, Jun Zhang *

School of Aeronautic Science and Engineering, Beihang University, Beijing 100191, China

ABSTRACT

The conjugate flow and heat transfer of phase change materials (PCMs)-metal foam confined between two annuli is addressed. A pulse heat load is employed at the inner surface of annuli, while the outer surface is subject to convection cooling. (This content of this sentence is the same as that in other sentences.) The enthalpy-porosity approach is utilized to model the phase change, and the natural convection in the porous medium is taken into account using Darcy-Brinkman model. The governing equations are transformed into non-dimensional form and solved by the finite element method. The finite element method is employed to solve the governing equations in the non-dimensional form. An automatic grid adaptation technique is employed to capture the phase change interface. The results are compared with theoretical and experimental studies available in the literature and found in good agreement. The steady-state solution and transient characteristics are addressed. The results demonstrate that the heatsink filled with PCM-metal foam can enhance the heat transfer at the hot surface, particularly at low external cooling power (Biot number < 0.2). The results reveal that the fusion temperature of phase change material is the key parameter on temperature controlling of the hot surface. Using the phase change heatsink results in a cooling power four times higher than that of pure external convection during the pulse load.

© 2019 Elsevier Ltd. All rights reserved.

1. Introduction

The phase change heat transfer has various practical applications in solar systems [1], building thermal management [2], solar cooker [3], sustainable drying of agricultural products [4], energy storage [5], and heatsinks [6,7]. The phase change heat transfer occurs on the melting/solidification of materials at their fusion temperature.

The Phase Change Materials (PCMs) can store/release a notable amount of thermal energy on solidification/melting at a constant fusion temperature. Therefore, PCMs are promising for thermal management of systems with transient heat loads. However, most PCMs have low thermal conductivity, which is the barrier to the utilization of these materials for thermal management of heat sinks. Recently, there have been significant advances on enhancing the thermal conductivity of PCMs by using nano-additives [8–10], fins [11,12], heat pipes [13,14], and metal foams [15–17].

In practice, the phase change materials are enclosed in containers to prevent leakage and ease of management. The containers can be in various shapes and designs, which depends on the applica-tion, production, and mechanical consideration. The melting/freez-ing phase-change heat transfer of PCMs in enclosures has been the subject of various recent studies. For example, Bondareva and Sheremet [18] addressed the melting heat transfer of PCMs in a cavity with a local heater. Using fins and nano additives are two popular approaches to enhancing the heat transfer of PCMs. Bon-dareva and Sheremet [19] investigated the effect of utilizing fins as heat transfer enhancers on phase change heat transfer of an enclosure phase change heatsink for electronics cooling applica-tions. The outcomes show that the required time for a complete melting is a function of the fins sizes. Bondareva et al. [20] exam-ined the effect of using alumina nanoparticles as heat transfer enhancers on the phase change behavior of phase change materials in a cavity heat sink. One of the most prominent disadvantages of using fins as heat transfer enhancer is the significant increases the heatsink weights. The effect of using nanoparticles [21] or hybrid nanoparticles [22,23] and magnetic field [24] are also investigated on the phase change heat transfer. The results show that using nanoparticles or hybrid nanoparticles can improve the melting heat transfer. Although using nano-additive can enhance the heat transfer of PCMS, the stability of PCMs with nano-additives is a problem in phase change cycles, and it demands future investigations.

---

* Corresponding author.
  E-mail address: jun.zhang@buaa.edu.cn (J. Zhang).

Nomenclature

Latin symbols

A	surface area of heat sink (m^2)
A_{mush}	constant with a large number
Bi	Biot number, $h_\infty(r_0 - r_i)/k_{m,l}$
C_p	heat capacity (J kg^{-1} K^{-1})
Da	Darcy number, $\kappa/(r_0 - r_i)^2$
e	constant with a small value
g	gravitational constant (m s^{-2})
h	convective heat transfer coefficient (W m^{-2} K^{-1})
h_{sf}	latent heat of fusion (J kg^{-1})
k	thermal conductivity (W m^{-1} K^{-1}), number of elements
MVF	normalized melt volume fraction
n	normal to a surface (m)
N	non-dimensional normal to a surface, total grid points
N	total grid pints, k
p	pressure (N m^{-2})
P	non-dimensional pressure
Pr	Prandtl number, $v/\alpha_{m,l}$
q''	(W m^2)
q_0''	heat flux at the hot surface (W m^{-2})
R	non-dimensional radial coordinate, $r/(r_0 - r_i)$
r	radial coordinate (m)
Ra	Rayleigh number, $(g\beta_l \Delta T(r_0 - r_i)^3)/(v_l \alpha_{m,l})$
r_i	inner radius of the cavity (m)
R_i	non-dimensional outer radius of cavity
r_o	outer radius of cavity (m)
R_o	non-dimensional inner radius of cavity
s	source term
S	non-dimensional source term
Ste	Stephan number, $((\rho C_p)_{m,l} \Delta T)/(\rho_l h_{sf,m})$
s_λ	non-dimensional perimeter of the hot surface, $\pi(R_i - \iota)$
t	time (s)
T	temperature (K)
u	x-velocity component (m s^{-1})
U	non-dimensional X-velocity component
v	y-velocity component (m s^{-1})
V	non-dimensional Y-velocity component
x	x-coordinate (m)
X	non-dimensional X-direction
y	y-coordinate (m)
Y	non-dimensional Y-direction

Greek symbols

α	thermal diffusivity (m^2 s^{-1})
β	volume expansion coefficient (K^{-1})
δ	non-dimensional heat flux
δt	heat pulse duration (s)
δT	phase change temperature range (K)
ΔT	temperature difference based on heat flux (K), $q''_0(r_o - r_i)/k_{m,l}$
$\delta\tau$	non-dimensional heat pulse duration
ε	porosity of the metal foam
η	heatsink efficiency
θ	non-dimensional temperature
ι	non-dimensional copper shell thickness
ι_0	thickness of the copper shields
κ	permeability of the metal foam (m^2)
λ	the non-dimensional tangential distance starting from point A
μ	dynamic viscosity (kg m^{-1} s^{-1})
v	kinematic viscosity (kg m^{-1} s^{-1})
ξ	power of heat load, the basis function of finite element method
ρ	density (kg m^{-3})
τ	non-dimensional time
ϕ	melt volume fraction
χ	a large number

Subscripts

0	initial steady-state solution
1	start of heat pulse
2	end of heat pulse
∞	external cooling flow
ave	average
b	hot surface
f	fusion
l	liquid/molten PCM
m	effective of the PCM and porous matrix
s	solid PCM
w	wall, copper shell

Recently, using metal foams for enhancing heat transfer properties of PCMs has attracted the attention of researchers. Nickel, aluminum, copper, and other high thermal conductive foams can be utilized as the porous matrix. The PCMs are embedded in the pores of the porous matrix, and as a result, an enhanced thermal conductive composite PCM-metal foam can be produced [17]. Metal foams are available with various porosities, pore size, and permeability. The presence of a porous matrix affects the fusion temperature, sensible heat capacity, and the latent heat of fusion of PCM-metal foam. Moreover, the presence of a porous medium weakens the natural convection flows, which is a significant drawback in the design of PCM enclosures.

The heat transfer without phase change in enclosures filled with porous media has been investigated in various studies during the past years. For instance, Sivasankaran et al. [25] studied the natural convection heat transfer in a wavy wall cavity filled with a porous medium. Alsabery et al. [26] examined the influence of a rotating solid cylinder on the convection heat transfer in a cavity. Chamkha and Selimefendigil [27] investigated the convection heat transfer in a porous cavity by considering the magnetohydrodynamic effects. The unsteady heat transfer [28], double diffusive effects

[29], cavity inclination angle [30], and Ferro-fluids subject to magnetic field effects [31] are addressed. The radiation effects in metal foams [32,33], including convective radiative [33] and local radiative conductivity [34] are also explored.

There are only a few studies that have addressed the phase change heat transfer in porous media. Xiao et al. [35] synthesized samples of paraffin-copper foam and paraffin-nickel foam composites. They utilized porous foams with various pore sizes and measured the thermophysical properties of the samples. The results show that the effective thermal conductivity of paraffin-metal foam was drastically enhanced, nearly three times larger than that of the pure paraffin. The porous matrix slightly shifts the phase change temperatures. The presence of the porous matrix also reduces the overall latent heat of phase change. Sheikholeslami [36] and Sheikholeslami et al. [37] modeled the solidification phase-change heat transfer in a cavity for thermal energy storage applications. Xu et al. [38] and Kohyani et al. [39] analyzed the melting heat transfer of phase change materials in a porous medium. Zheng et al. [40] experimentally examined the melting phase change behavior of paraffin wax in a copper metal foam porous medium. The porosity of the metal foam was 0.95, and the pores

were fully saturated with the paraffin wax. The outcomes reveal that the total melting time in the case of using copper metal foam was 20.5% shorter than that of pure paraffin. Giorgio et al. [41] utilized a local thermal non-equilibrium porous model and investigated the melting heat transfer in a metal foam. Mancin et al. [42] experimentally examined the melting of paraffin waxes in a copper metal foam. It was found that the copper foams notably improves the heat transfer performance of PCM.

In all the aforementioned studies [36–39,42], the heat load was steady and constant. However, there are some applications such as solar collectors, electronic devices, satellites, and batteries where the thermal load of the device flows a cyclic or a transient behavior. For example, Hussain et al. [43] experimentally investigated the thermal loads of a battery in charging and discharging processes and utilized a paraffin-nickel foam composite package to manage the transient thermal demands of the battery. The phase change heat transfer subject to transient or cyclic loads involves both melting and solidification phase change.

To the best of our knowledge, the effect of using a transient heat load on the phase change behavior of PCM-metal foam has not been addressed yet. The present study aims to theoretically address the phase change heat transfer of phase change materials in metal foams subject to a transient heat load. The transient phase change heat transfer involves both melting and solidification process, and it is critically important for thermal management and energy storage management of systems with variable heat loads.

The present study aims to answer the following fundamental questions: Does the use of PCM-metal foam enhances the heat transfer for a transient load?; Does the use of PCM-metal foam increases the steady-state temperature of the hot surface?; Is there any equilibrium situation for a regular steady load?; 4- How does PCM-metal foam react to the pulse heat load by melting/solidification? To address the above fundamental questions on the design of PCM-metal foam, the modeling approach and simulation method will be introduced in the following sections.

2. Mathematical model

2.1. Physical model

Fig. 1(a) depicts the annuli space between two horizontal cylinders filled with metal foam and saturated by a PCM. The metal foam is a porous medium with the porosity of ε and permeability of κ. The thickness of the inner and outer cylinders is ι_0. The inner cylinder contains a battery which produces a variable surface heat flux, $q''(t)$. The outer cylinder is cooled by convection with the ambient temperature of T_∞ and convection heat transfer coefficient of h_∞. The fusion temperature of PCM is T_f where $T_f > T_\infty$. The produced heat flux of the battery is in the form of a transient pulse heat flux, as depicted in Fig. 1(c). The heat load is low as $q''(t) = q_0''$ for a long time, and the heat transfer in the heatsink is steady state. At the initial time of t_0, the heat flux suddenly raises to a high value of $q''(t) = q_0''(1 + \xi)$ and continues until the time t_1. During the interval time of t_0 to t_1, the melting occurs by absorbing the heat flux. At the time of $t = t_1$ the flux reduces to $q''(t) = q_0''$ and after while the solidification process occurs to charge the heatsink. Following the study of Hussain et al. [43], it is assumed that the metal foam is made of Nickel foam, and the PCM is paraffin wax. The cylinders are assumed to be made of copper.

2.2. Governing equations

The governing equations in the 2-D Cartesian system for the continuity, momentum in the porous medium, and heat transfer with phase change are [44–46]:

$$\frac{\partial u}{\partial x} + \frac{\partial v}{\partial y} = 0 \tag{1}$$

$$\frac{\rho_l}{\varepsilon}\frac{\partial u}{\partial t} + \frac{\rho_l}{\varepsilon^2}\left(u\frac{\partial u}{\partial x} + v\frac{\partial u}{\partial y}\right) = -\frac{\partial p}{\partial x} + \frac{\mu_l}{\varepsilon}\left(\frac{\partial^2 u}{\partial x^2} + \frac{\partial^2 u}{\partial y^2}\right) - \frac{\mu_l}{\kappa}u - s(T)u \tag{2}$$

$$\frac{\rho_l}{\varepsilon}\frac{\partial v}{\partial t} + \frac{\rho_l}{\varepsilon^2}\left(u\frac{\partial v}{\partial x} + v\frac{\partial v}{\partial y}\right) = -\frac{\partial p}{\partial y} + \frac{\mu_l}{\varepsilon}\left(\frac{\partial^2 v}{\partial x^2} + \frac{\partial^2 v}{\partial y^2}\right) - \frac{\mu_l}{\kappa}v$$
$$- s(T)v + \rho_l g\beta_l(T - T_\infty) \tag{3}$$

Energy in PCM-metal foam:

$$(\rho C_p)_m\frac{\partial T}{\partial t} + (\rho C_p)_l\left(u\frac{\partial T}{\partial x} + v\frac{\partial T}{\partial y}\right)$$
$$= k_m\left(\frac{\partial^2 T}{\partial x^2} + \frac{\partial^2 T}{\partial y^2}\right) - \rho_l h_{sf,m}\frac{\partial \phi(T)}{\partial t} \tag{4}$$

Energy in Solid Copper parts (Fin and cylinder walls):

$$(\rho C_p)_w\frac{\partial T}{\partial t} = k_w\left(\frac{\partial^2 T}{\partial x^2} + \frac{\partial^2 T}{\partial y^2}\right) \tag{5}$$

where $(\rho C_p)_m$ is the heat capacity of PCM- metal foam, $(\rho C_p)_l$ is the heat capacity of the liquid paraffin, and $(\rho C_p)_w$ is the heat capacity of the copper wall. $h_{sf,m}$ is the effective latent heat of phase change. The effective latent heat of phase change is calculated for the paraffin wax inside the pores as $h_{sf,m} = \varepsilon h_{sf}$. Here, k_m and k_w are the effective thermal conductivity of PCM- metal foam and the thermal conductivity of cylinder walls, respectively.

Although there are various relations for evaluating the effective heat capacity and effective thermal conductivity of the porous medium and the PCM inside the pores, most of the relations are not much accurate. Considering paraffin as the phase change material and nickel as metal foam, the actual experimental data are utilized for the effective thermal conductivity of paraffin-nickel metal foam reported by Xiao et al. [35]. Xiao et al. [35] systemized different samples of paraffin-nickel metal foam and measured the thermophysical properties of the samples.

The thermophysical properties of paraffin (PCM), nickel (metal foam), and copper (solid wall) are summarized in Table 1. The permeability of the porous medium with 10PPI pore size and porosity of $\varepsilon \sim 0.95$ (which is close to the porosity and pore size of the present study) is adopted from experiment study of Bhattacharya et al. [47] as $\kappa = 1.2 \times 10^{-7}$ m^2. The heat capacity of the pure liquid paraffin is $(\rho C_p)_l = 1627.2$ kJ/kg [35]. The heat capacity and thermal conductivity of the copper are $(\rho C_p)_w = 3435.4$ (kJ/kg), [40], and $k_w = 360$ (W/m K).

The term $s(T)$ forces the velocities in the momentum equation to zero in the solid PCMs. It is assumed that the phase change occurs in the range of δT where $\phi(T)$ introduces the melting fraction in the melting interval. The source terms of $s(T)$ and $\phi(T)$ are introduced as:

$$s(T) = A_{mush}\frac{(1 - \phi(T))^2}{\phi(T)^3 + e} \tag{6a}$$

$$\phi(T) = \begin{cases} 0 & T < T_f - \frac{\delta T}{2} \\ \frac{T - T_f}{\delta T} + \frac{1}{2} & T_f - \frac{\delta T}{2} < T < T_f + \frac{\delta T}{2} \\ 1 & T > T_f + \frac{\delta T}{2} \end{cases} \tag{6b}$$

wherein the above equations e is a small number equal to 10^{-3} which prevents the denominator of term $s(T)$ to become zero when $\phi = 0$. A_{mush} is a large number, here $A_{mush} = 5 \times 10^5$, which forces the
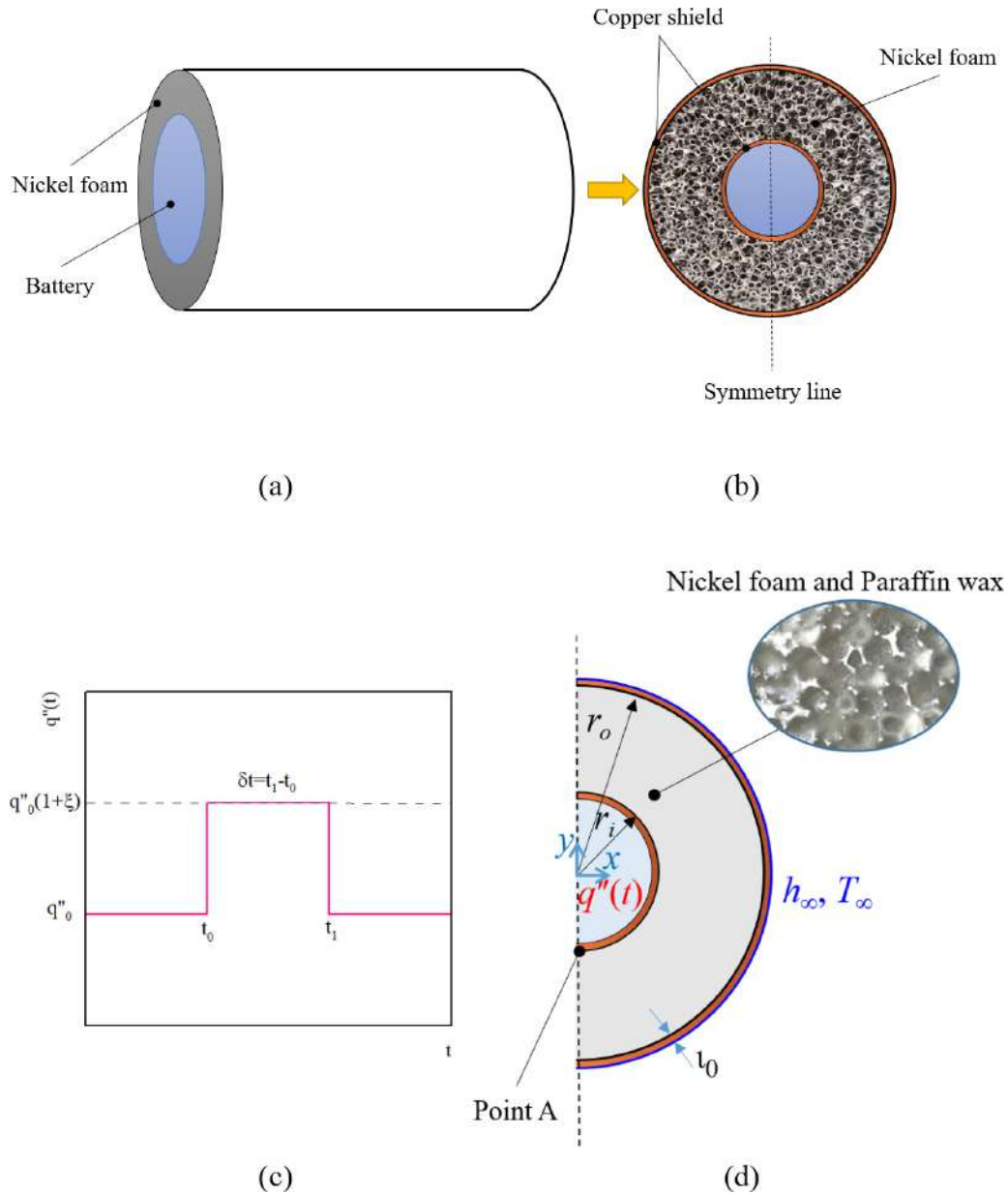
Fig. 1. Schematic view of heatsink filled with PCM-metal foam: (a): A 3D view of model; (b): 2D view of model; (c): The pulse heat flux; (d): The boundary conditions and coordinate system.

Table 1
The thermophysical properties of materials [35,40,48].

Property	Paraffin Liquid	Paraffin solid	Nickel	Copper
k (W/m K)	0.3	0.3	91.4	380
ρ (kg/m^3)	769	914	8900	8930
C_p (J/kg K)	2116	1959	502.4	386

velocities of the momentum equation to zero in solid regions, i.e., $\phi \rightarrow 0$.

In Eq. (6b), when the temperature is lower than the fusion temperature, i.e., $T < T_f - \delta T/2$, the paraffin wax is in the solid-state, and when the temperature is higher than $T > T_f + \delta T/2$, the paraffin wax is in the liquid state. Finally, when the temperature is in the phase change interval, $T_f - \delta T/2 < T < T_f + \delta T/2$, the liquid fraction changes linearly. The following relation for the effective heat capacity of the porous medium and PCM is utilized:

$$(\rho C_p)_m = \phi (\rho C_p)_{m,l} + (1 - \phi)(\rho C_p)_{m,s} \qquad (7)$$

where $(\rho C_p)_{m,l}$ and $(\rho C_p)_{m,s}$ are the effective heat capacity of liquid paraffin-nickel foam and solid paraffin-nickel foam, respectively.

The boundary conditions are as follow:

The inner wall of the inner cylinder is subject to heat flux as:

$$k_w \frac{\partial T}{\partial n}\bigg)_{r=r_{i-l}} = q''(t) \qquad (8a)$$

where the normal vector of the surface is denoted by n. Convection heat transfer at the outer cylinder:

$$k_w \frac{\partial T}{\partial n}\bigg)_{r=r_o+\iota} = h_\infty (T - T_\infty) \tag{8b}$$

The energy balance and temperature continuity at the interface of the solid copper parts and the PCM-metal foam:

$$T|_{wall} = T|_{metal\,foam} \ and \ k_w \frac{\partial T}{\partial n}\bigg|_{wall} = k_m \frac{\partial T}{\partial n}\bigg|_{metal\,foam} \tag{8c}$$

The zero velocity boundary conditions at the interface of the solid walls and PCM-metal foam is assumed as:

$$u = v = 0 \tag{8d}$$

A reference pressure with $p = 0$ is adopted at the interface of PCM-metal foam next to the bottom of the inner solid wall (Point A).

At the symmetry line ($x = 0$):

$$\frac{\partial T}{\partial x} = \frac{\partial v}{\partial x} = 0 \tag{8e}$$

As the initial condition, it is assumed the entire of the heatsink is at a uniform ambient temperature of T_∞. Then, the battery turns on with low heat flux of $q''(t) = q_0''$ for a long time until the heat sink reaches to a steady-state heat transfer and temperature distribution. Then, after a time t_0 the power of element raises to $q''(t) = q_0''(1 + \xi)$ and remains constant until t_2. After that, the power of element reduces to $q''(t) = q_0''$. Therefore, the flow field and temperature field at $t = 0$ are the steady-state flow and temperature fields for an element with the power of $q''(t) = q_0''$.

In order to generalize the solution, governing equations of Eqs. (1)–(5) are transformed into a non-dimensional form by introducing the following non-dimensional parameters:

$$X = \frac{x}{r_o - r_i}, Y = \frac{y}{r_o - r_i}, R_i = \frac{r_i}{r_o - r_i}, R_o = \frac{r_o}{r_o - r_i}, \iota = \frac{\iota_0}{r_o - r_i}, U = \frac{u(r_o - r_i)}{\alpha_{m,l}},$$

$$V = \frac{v(r_o - r_i)}{\alpha_{m,l}}, \theta = \frac{T - T_\infty}{\Delta T}, \tau = \frac{t\alpha_{m,l}}{(r_o - r_i)^2}, S(\theta) = \frac{s(T)(r_o - r_i)^2}{\rho_l \alpha_{m,l}}, Da = \frac{\kappa}{(r_o - r_i)^2}$$

$$P = \frac{p(r_o - r_i)^2}{\rho \alpha_{m,l}^2}, \alpha_{m,l} = \frac{k_{m,l}}{(\rho c_p)_{m,l}}, \Pr = \frac{v}{\alpha_{m,l}}, Ra = \frac{g\beta_l \Delta T(r_o - r_i)^3}{v_l \alpha_{m,l}}, Ste = \frac{(\rho C_p)_{m,l}\Delta T}{\rho_l h_{sf,m}} \tag{9}$$

where $r_o - r_i$ is the characteristic length and $\alpha_{m,l} = k_{m,l}/(\rho C_p)_{m,l}$. Here, Pr, Ra, and Ste are the Prandtl number, the Rayleigh number, and the Stephan number, respectively. The temperature scale ΔT is defined based on the battery heat flux of q_0'' as $\Delta T = q_0''(r_o - r_i)/k_{m,l}$. The values of $k_m/k_{m,l}$ is considered as unity for convenience. This means that the effective thermal conductivity of the porous matrix and liquid PCM is the same as that of porous matrix and solid PCM. Invoking the non-dimensional parameters of Eqs. (9) and (7), the governing equations, Eqs. (1)–(5), are written in the following non-dimensional form:

$$\frac{\partial U}{\partial X} + \frac{\partial V}{\partial Y} = 0 \tag{10}$$

$$\frac{1}{\varepsilon}\frac{\partial U}{\partial \tau} + \frac{1}{\varepsilon^2}\left(U\frac{\partial U}{\partial X} + V\frac{\partial U}{\partial Y}\right) = -\frac{\partial P}{\partial X} + \frac{\Pr}{\varepsilon}\left(\frac{\partial^2 U}{\partial X^2} + \frac{\partial^2 U}{\partial Y^2}\right) - \frac{\Pr}{Da}U$$
$$- S(\theta)U \tag{11}$$

$$\frac{1}{\varepsilon}\frac{\partial V}{\partial \tau} + \frac{1}{\varepsilon^2}\left(U\frac{\partial V}{\partial X} + V\frac{\partial V}{\partial Y}\right) = -\frac{\partial P}{\partial Y} + \frac{\Pr}{\varepsilon}\left(\frac{\partial^2 V}{\partial X^2} + \frac{\partial^2 V}{\partial Y^2}\right) - \frac{\Pr}{Da}V$$
$$- S(\theta)V + \Pr Ra\theta \tag{12}$$

$$\left(\phi + (1 - \phi)\frac{(\rho C p)_{m,s}}{(\rho C_p)_{m,l}}\right)\frac{\partial \theta}{\partial \tau} + \frac{(\rho C_p)_l}{(\rho C_p)_{m,l}}\left(U\frac{\partial \theta}{\partial X} + V\frac{\partial \theta}{\partial Y}\right)$$
$$= \left(\frac{\partial^2 \theta}{\partial X^2} + \frac{\partial^2 \theta}{\partial Y^2}\right) - \frac{1}{Ste}\frac{\partial \phi(\theta)}{\partial \tau} \tag{13}$$

$$\frac{(\rho C_p)_w}{(\rho C_p)_{m,l}}\frac{\partial \theta}{\partial \tau} = \left(\frac{k_w}{k_{m,l}}\right)\left(\frac{\partial^2 \theta}{\partial X^2} + \frac{\partial^2 \theta}{\partial Y^2}\right) \tag{14}$$

In Eq. (13), the source $\phi(\theta)$ is:

$$\phi(\theta) = \begin{cases} 0 & \theta < \theta_f - \frac{1}{2}\delta\theta \\ \frac{\theta - \theta_f}{\delta\theta} + \frac{1}{2} & \theta_f - \frac{1}{2}\delta\theta < \theta < \theta_f + \frac{1}{2}\delta\theta \\ 1 & \theta > \theta_f + \frac{1}{2}\delta\theta \end{cases} \tag{15}$$

where $\theta_f = (T_f - T_\infty)/\Delta T$. Accordingly, the non-dimensional boundary conditions are obtained as:

$$\frac{k_w}{k_{m,l}}\frac{\partial \theta}{\partial N}\bigg)_{R=R_i-\iota} = \delta(\tau) \tag{16a}$$

where $\delta(\tau) = \begin{cases} 1 + \xi & \tau_0 < \tau < \tau_1 \\ 1 & \tau < \tau_0, \ \tau > \tau_1 \end{cases}, \tau_0 = \frac{t_0 \alpha_{m,l}}{(r_o - r_i)^2}, \tau_1 = \frac{t_1 \alpha_{m,l}}{(r_o - r_i)^2}.$

$$\frac{k_w}{k_{m,l}}\frac{\partial T}{\partial N}\bigg)_{R=R_o+\iota} = Bi\theta_w \tag{16b}$$

where $Bi = h_\infty (r_0 - r_i)/k_{m,l}$ and $\theta_w = (T_w - T_\infty)/\Delta T$.

$$\theta_{wall} = \theta|_{metal\,foam} \ and \ \frac{k_w}{k_{m,l}}\frac{\partial \theta}{\partial N}\bigg|_{wall} = \frac{k_m}{k_{m,l}}\frac{\partial \theta}{\partial N}\bigg|_{metal\,foam} \tag{16c}$$

At the interface of the solid walls and PCM-metal foam $U = V = 0$
$$\tag{16d}$$

At the symmetry line ($X = 0$) : $\frac{\partial \theta}{\partial X} = \frac{\partial V}{\partial X} = 0$ $\tag{16e}$

The non-dimensional reference pressure, at Point A, is obtained as $P = 0$. As the initial solution, $\theta = 0$, and $\delta(\tau) = 1$ for a long time until the heatsink reaches to a steady-state. Therefore, the non-dimensional flow and temperature fields at $\tau = 0$ will be the steady state solution for $\delta(\tau) = 1$.

The characteristic parameter of interest is the temperature of the battery surface where the heat flux was imposed, i.e., $r = r_i - \iota_0$. The dimensionless local temperature at the battery surface is defined as:

$$\theta_{b,\lambda} = \frac{T_{b,\lambda} - T_\infty}{\Delta T} \ at\, R = R_i - \iota \tag{17}$$

where λ is the non-dimensional tangential distance starting from point A. The average surface temperature is evaluated by integration over the local temperature over the length of the battery surface and divided by the overall length of the surface (s):

$$\theta_{b,ave} = \frac{\int_0^{s_\lambda} \theta_b d\lambda}{s} \tag{18}$$

where $s_\lambda = \pi(R_i - \iota)$.

If assuming the battery is cooled by ambient (in the absence of heatsink), the surface temperature of the battery can be computed using the energy balance as:

$$q''(t) = h_\infty (T_b - T_\infty) \tag{19}$$

Using the non-dimensional Eq. (10), the energy balance of Eq. (20) is obtained in the following non-dimensional form:

$$\theta_{b,0} = \frac{\delta(\tau)}{Bi} \tag{20}$$

Using the average battery temperature in the presence ($\theta_{b,ave}$) and the absence ($\theta_{b,0}$) of the heatsink, the heatsink efficiency can be introduced as the following ratio:

$$\eta = \frac{\theta_{b,0}}{\theta_{b,ave}} = \frac{\delta(\tau)}{\theta_{b,ave} Bi} \tag{21}$$

The normalized Melt Volume Fraction (*MVF*) is introduced as the ratio of melt in the enclosure to the ratio of total void space filled with paraffin as:

$$MVF = \frac{\int_A \varepsilon \phi dA}{\int_A \varepsilon dA} \tag{22}$$

where $\int_A \varepsilon dA = \varepsilon \pi \left(R_o^2 - R_i^2 \right)$

3. Numerical method

Utilizing an efficient numerical approach to solve the non-linear partial differential equations in a coupled form is necessary. The governing equation through the temperature field are fully coupled and extremely non-linear. The finite element method based on the Galerkin technique is considered to solve the governing equations. More details about the utilized numerical method can be found in [49–51]. The pressure term in momentum equations was eliminated by a penalty function defined as follow:

$$P = \chi \left(\frac{\partial U}{\partial X} + \frac{\partial V}{\partial Y} \right) \tag{24}$$

It is known that the continuity equation is satisfied, if χ, namely penalty number, is a large value. Substituting this penalty function for pressure term gives the following equations:

$$\frac{1}{\varepsilon} \frac{\partial U}{\partial \tau} + \frac{1}{\varepsilon^2} \left(U \frac{\partial U}{\partial X} + V \frac{\partial U}{\partial Y} \right) = -\frac{\partial}{\partial X} \left(\chi \left(\frac{\partial U}{\partial X} + \frac{\partial V}{\partial Y} \right) \right) + \frac{Pr}{\varepsilon} \left(\frac{\partial^2 U}{\partial X^2} + \frac{\partial^2 U}{\partial Y^2} \right) - \frac{Pr}{Da} U - S(\theta) U \tag{25}$$

$$\frac{1}{\varepsilon} \frac{\partial V}{\partial \tau} + \frac{1}{\varepsilon^2} \left(U \frac{\partial V}{\partial X} + V \frac{\partial V}{\partial Y} \right) = -\frac{\partial}{\partial Y} \left(\chi \left(\frac{\partial U}{\partial X} + \frac{\partial V}{\partial Y} \right) \right) + Pr \left(\frac{\partial^2 V}{\partial X^2} + \frac{\partial^2 V}{\partial Y^2} \right) - \frac{Pr}{Da} V - S(\theta) V + Pr Ra \theta \tag{26}$$

Employing a basis set $\{\xi_k\}_{k=1}^N$, the velocity components, and the temperature can be expanded such as:

$$U \approx \sum_{k=1}^N U_k \xi_k(X,Y), V \approx \sum_{k=1}^N V_k \xi_k(X,Y), \theta \approx \sum_{k=1}^N \theta_k \xi_k(X,Y) \tag{27}$$

The use of Galerkin finite element approach results in the non-linear residuals as below:

$$R_i^1 \approx \frac{1}{\varepsilon} \sum_{k=1}^N U_k \int \frac{\partial \xi_k}{\partial \tau} \xi_i dXdY + \frac{1}{\varepsilon^2} \sum_{k=1}^N U_k \int \left[\left(\sum_{k=1}^N U_k \xi_k \right) \frac{\partial \xi_k}{\partial X} + \left(\sum_{k=1}^N V_k \xi_k \right) \frac{\partial \xi_k}{\partial Y} \right] \xi_i dXdY$$

$$+ \gamma \left[\sum_{k=1}^N U_k \int \frac{\partial \xi_i}{\partial X} \frac{\partial \xi_k}{\partial X} dXdY + \sum_{k=1}^N V_k \int \frac{\partial \xi_i}{\partial X} \frac{\partial \xi_k}{\partial Y} dXdY \right]$$

$$+ Pr \sum_{k=1}^N U_k \int \left[\frac{\partial \xi_i}{\partial X} \frac{\partial \xi_k}{\partial X} + \frac{\partial \xi_i}{\partial Y} \frac{\partial \xi_k}{\partial Y} \right] dXdY - \frac{Pr}{Da} \int \left(\sum_{k=1}^N U_k \xi_k \right) \xi_i dXdY$$

$$- S(\theta) \int \left(\sum_{k=1}^N U_k \xi_k \right) \xi_i dXdY \tag{28}$$

$$R_i^2 \approx \frac{1}{\varepsilon} \sum_{k=1}^N V_k \int \frac{\partial \xi_k}{\partial \tau} \xi_i dXdY + \frac{1}{\varepsilon^2} \sum_{k=1}^N V_k \int \left[\left(\sum_{k=1}^N U_k \xi_k \right) \frac{\partial \xi_k}{\partial X} + \left(\sum_{k=1}^N V_k \xi_k \right) \frac{\partial \xi_k}{\partial Y} \right] \xi_i dXdY$$

$$+ \gamma \left[\sum_{k=1}^N U_k \int \frac{\partial \xi_i}{\partial Y} \frac{\partial \xi_k}{\partial X} dXdY + \sum_{k=1}^N V_k \int \frac{\partial \xi_i}{\partial Y} \frac{\partial \xi_k}{\partial Y} dXdY \right]$$

$$+ Pr \sum_{k=1}^N V_k \int \left[\frac{\partial \xi_i}{\partial X} \frac{\partial \xi_k}{\partial X} + \frac{\partial \xi_i}{\partial Y} \frac{\partial \xi_k}{\partial Y} \right] dXdY - Ra Pr \int \left(\sum_{k=1}^N \theta_k \xi_k \right) \xi_i dXdY$$

$$- \frac{Pr}{Da} \int \left(\sum_{k=1}^N V_k \xi_k \right) \xi_i dXdY - S(\theta) \int \left(\sum_{k=1}^N V_k \xi_k \right) \xi_i dXdY \tag{29}$$

$$R_i^3 \approx \left(\phi + (1-\phi) \frac{(\rho Cp)_{m,s}}{(\rho Cp)_{m,l}} \right) \sum_{k=1}^N \theta_k \int \frac{\partial \xi_k}{\partial \tau} \xi_i dXdY$$

$$+ \frac{(\rho C_p)_l}{(\rho C_p)_{m,l}} \sum_{k=1}^N \theta_k \int \left[\left(\sum_{k=1}^N U_k \xi_k \right) \frac{\partial \xi_k}{\partial X} + \left(\sum_{k=1}^N V_k \xi_k \right) \frac{\partial \xi_k}{\partial Y} \right] \xi_i dXdY \tag{30}$$

$$+ \sum_{k=1}^N \theta_k \int \left[\frac{\partial \xi_i}{\partial X} \frac{\partial \xi_k}{\partial X} + \frac{\partial \xi_i}{\partial Y} \frac{\partial \xi_k}{\partial Y} \right] dXdY - \frac{1}{Ste} \sum_{k=1}^N \phi(\theta_k) \int \frac{\partial \xi_k}{\partial \tau} \xi_i dXdY$$

Linear discrimination is adopted for the heat equation. A grid adaptation approach is utilized to capture the phase change interface. The grid adaptation region is estimated base on the phase change area with the phase change volume-fraction in the range of [0.05; 0.095].

The time step is also controlled automatically using the Backward Differentiation Formula (BDF) with a free time steps scheme within a minimum BDF order of one, and a maximum BDF order of two [52]. A PARDISO solver [53,54] associated with the Newton method are utilized to solve the residual equations with the damping factor of 0.9. The residual equations were solved iteratively until the absolute residual error of the equations reached below 10^{-6} at each time step.

4. Grid check and validation

4.1. Value of non-dimensional parameters

A cylindrical enclosure with r_i = 10 mm and r_o = 30 mm and the wall copper thickness of l_0 = 1 mm is adopted as a practical case. The enclosure is filled with nickel-metal foam (with a pore size of 10 PPI and porosity of ε = 0.975) and saturated with paraffin wax. The outer cylinder is exposed to the ambient air with the convective heat transfer coefficient of h_∞ = 25 (W/m K), and the ambient temperature of T_∞ = 14 °C. As mentioned, the permeability of the porous medium is κ = 2.7 × 10^{-7} m^2 [47], and the effective thermal conductivity of the porous matrix and the material inside the pores, nickel foam, and paraffin wax is k_m = 1 (W/m K) [35] and as mentioned $k_{m,s} = k_{m,l} = k_m$. The battery produces heat in the form of surface heat flux with the flux power of q_0'' = 1500 (W/m^2) at the inner surface of the inner cylinder, at $r = r_i - l_0$. The thermophysical properties of the copper wall, paraffin wax, and nickel structure are reported in the modeling section. It is assumed that the battery produces the surface heat flux with an excessive rate of γ = 3 during a δt = 1200 s discharge load. The discharging commences at the t_0 = 200 s and continues to t_1 = 1400 s.

The non-dimensional parameters corresponding to the above test case are computed as follows: Ra = 4.6728 × 10^{+5}, Da = 3.0 × 10^{-4}, Pr = 7.046, Bi = 0.5, ε = 0.975, θ_f = 1.5122, γ = 3, R_i = 0.5, R_o = 1.5, $(\rho C_p)_{m,s}/(\rho C_p)_{m,l}$ = 1.095, $(\rho C_p)_w/(\rho C_p)_{m,l}$ = 2.061, $k_w/k_{m,l}$ = 360, τ_0 = 0.299, and $\delta\tau$ = 1.794. The results of the present study will be reported for these non-dimensional parameters; otherwise, it will be stated.

4.2. Grid check

As mentioned in the modeling section, the phase change occurs at a very small temperature range, i.e., $\delta\theta$. Hence, the phase change occurs in a very narrow region in space because of the presence of high-temperature gradients due to convection flow and low thermal conductivity of the phase change medium. In this narrow region, the velocities change from free convection velocities in the liquid region to zero in the solid region. The latent heat of fusion will be released or absorbed, and the thermophysical properties are also changing from the liquid to solid. Hence, many changes occur in a very narrow region of space. Capturing all of the aspects of phase change at the melting interface with a regular fixed grid size is not possible and results in an unstable solution.

Therefore, in the present study, a grid adaptation technique is employed to capture the melting interface with a high resolution. The melting volume fraction ϕ controls the grid adaptation. During the grid adaptation, the size of the grids drops to 5 fold smaller than the domain grids with the growing ratio of 5.

In order to study the effect of the grid-size on the results, the calculations were repeated using several grid sizes. The details of the utilized grids are summarized in Table 2. The size of the grids at the interface of the solid and liquid-porous matrix at the inner cylinder is denoted by Boundary Interface Grid Size (BIGS). The grid size in the domain of solution is denoted by Domain of Solution Grid Size (DSGS). In all cases, the maximum growth rate of an element was 1.15. The total element is the number of triangular elements before adaptation.

Table 3 shows the average temperature of the hot surface ($\theta_{b,ave}$) for various values of the surface cooling power of the Biot number (Bi) and grid sizes. The results are reported for the steady-state solution with no pulse heat flux. As seen, the gird of case III provides adequate accuracy up to three significant digits. This table also shows that the increase of surface cooling power from $Bi = 0.2$ to $Bi = 0.5$ reduces the temperature of the hot surface from $\theta_{b,ave} = 1.83$ to $\theta_{b,ave} = 1.08$.

Fig. 2(a and b) illustrate the effect of grid size on the melt volume fraction (MVF) and the hot surface temperature profiles ($\theta_{b,ave}$), respectively. Fig. 2(c) depicts the melting interface at non-dimensional time $\tau = 2.093$, which is the end of the heat pulse. As seen, the results are almost independent of the grid size. Only Case I, with a coarse grid size, shows a slight grid dependency. Considering the results of Table 3 and Fig. 2, Grid IV is adopted for the future computations of the present study. Fig. 3 shows a general view of the utilized Grid IV with two magnified views over the grid for better illustration. Fig. 4 depicts the adapted grid at $\tau = 2.093$. The melting interface is depicted in Fig. 2(c) when $\tau = 2.093$. As seen in Fig. 4, the grid is adapted around the melting interface. Two magnified views of the grid are also depicted in Fig. 4 for clarification. The melt region and the solid region are depicted by light green and blue, respectively. The melting interface, $\phi = 0.5$, is plotted with a continues red curve.

4.3. Validations

The accuracy and correctness of the utilized code and modeling are validated by comparing the results with experimental and numerical works available in the literature. As the first comparison, the results of the present code are compared with the experimental results of Kumar et al. [55]. Kumar et al. [55] investigated the melting heat transfer of lead in a rectangular cavity. They utilized X-ray to capture the melting interface during the melting process. In the study of Kumar et al. [55], the left wall was subject to uniform heat flux, and the other walls were insulated. The results are obtained for a case with element heat flux of 16.3 kW/m^2, $Pr = 0.0236$, $Ste = 0.4$, $Ra = 1.4 \times 10^7$. The temperature at the element surface was measured 599 K. The right wall temperature was 555 K. Fig. 5 illustrates a comparison between the molten regions and solid regions reported by Kumar et al. [55] and the results obtained in the present study. As seen, the results of the present study are in full agreement with the experimental results of Kumar et al. [55] for melting in a cavity with no porous medium.

Considering another case with no porous medium, a comparison between the numerical and experimental results available in the literature and the present study is performed in Fig. 6 for melting of pure gallium. The non-dimensional parameters were $Ra = 6 \times 10^5$, $Pr = 0.0216$, $Ste = 0.039$ and aspect ratio of 0.714 (Height/Length). It should be noted that the Rayleigh number and Prandtl number were introduced based on the constant temperature of the hot wall as $\Delta T = (T_h - T_f)$. The left wall of the cavity was at a constant hot temperature, and the other walls were insulated. The results of the present work are compared with the experimental study of Gau and Viskanta [56] and the numerical results of Khodadadi and Hosseinizadeh [57], Kashani et al. [58], Tiari et al. [13], and Brent et al. [59]. Fig. 6 shows that the melting interface can vary notably by using different numerical methods. The reason is that the melting occurs at a constant temperature, and hence, a large value of A_{mush} parameter and a narrow band of $\delta\theta$ is required to capture the melting interface sharply. However, using a large value of A_{mush} and narrow band of $\delta\theta$ results in a discontinuity in the governing equations. An extremely high-quality grid and a stable solver is required to capture the melting interface correctly. Due to this fact, the adaptive mesh is utilized in for transient numerical solution of the present study to robustly capture the melting interface with miniature grids at the melting interface, and regular larger grids are the remaining domain of solution.

Fig. 6 shows good agreement with the results of the present study and the experimental results of Gau and Viskanta [56]. The difference between the numerical method and the experimental data can be due to the measuring technique in the study of Gau and Viskanta. Gau and Viskanta [56] utilized a mechanical probe to capture the melting interface. At the onset of the phase change, the melting interface can be unstable, and measuring the interface using a mechanical probe can affect the melting process and accurate capture of the shape of the interface.

In the case of steady-state heat transfer in a square cavity filled by a porous medium with no phase change, a comparison between the average Nusselt number reported in the literature and the present study is summarized in Table 4. The results are for a cavity with heated isothermal side walls with temperature difference while the top and bottom walls are insulated. Considering a small value of Darcy number, neglecting the viscous terms and assuming slip boundary condition at the walls, the porous media model in the present study will reduce to the regular Darcy model, and $Ra \times Da$ will be the same as the Darcy-Rayleigh number utilized in Darcy models of the literature studies. In this case, the results will be independent of the porosity and Prandtl number. A comparison between the results of the present study and the literature studies is performed in Table 4 with the same grid-size as adopted for the computations of the work.

As the final validation, the experimental results of Zheng et al. [40] for melting of paraffin wax in a copper foam is selected. Zheng et al. [40] investigated the melting of paraffin wax in a 10 cm cavity filled with copper metal foam of pore size 5 PPI and saturated with paraffin wax. The cavity with a porosity of $\varepsilon = 0.95$ was subject to a heat flux of $q = 1150$ W/m^2 from the top while the other walls were insulated. It is assumed that 7.5% of the element heat flux losses to the environment. The thermophysical properties are summarized in Table 5.

Based on the experimental measurements of Xiao et al. [35], the effective thermal conductivity of copper metal foam and paraffin

Table 2
The details of the utilized grids for grid check.

	Case I	Grid II	Grid III	Grid IV	Grid V
BIGS	0.07	0.095	0.0434	0.02015	0.0104
DSGS	0.135	0.104	0.07	0.0545	0.0434
Total elements	1196	1554	2310	4472	11,078

Table 3
The average non-dimensional temperature ($\theta_{b,ave}$) for various values of Biot number (Bi) and different grid sizes.

Bi	Grid I	Grid II	Grid III	Grid IV	Grid V
0.2	1.8214	1.8221	1.8254	1.8264	1.8274
0.3	1.4606	1.4610	1.4619	1.4620	1.4622
0.4	1.2189	1.2192	1.2200	1.2201	1.2202
0.5	1.0738	1.0741	1.0749	1.0749	1.0751
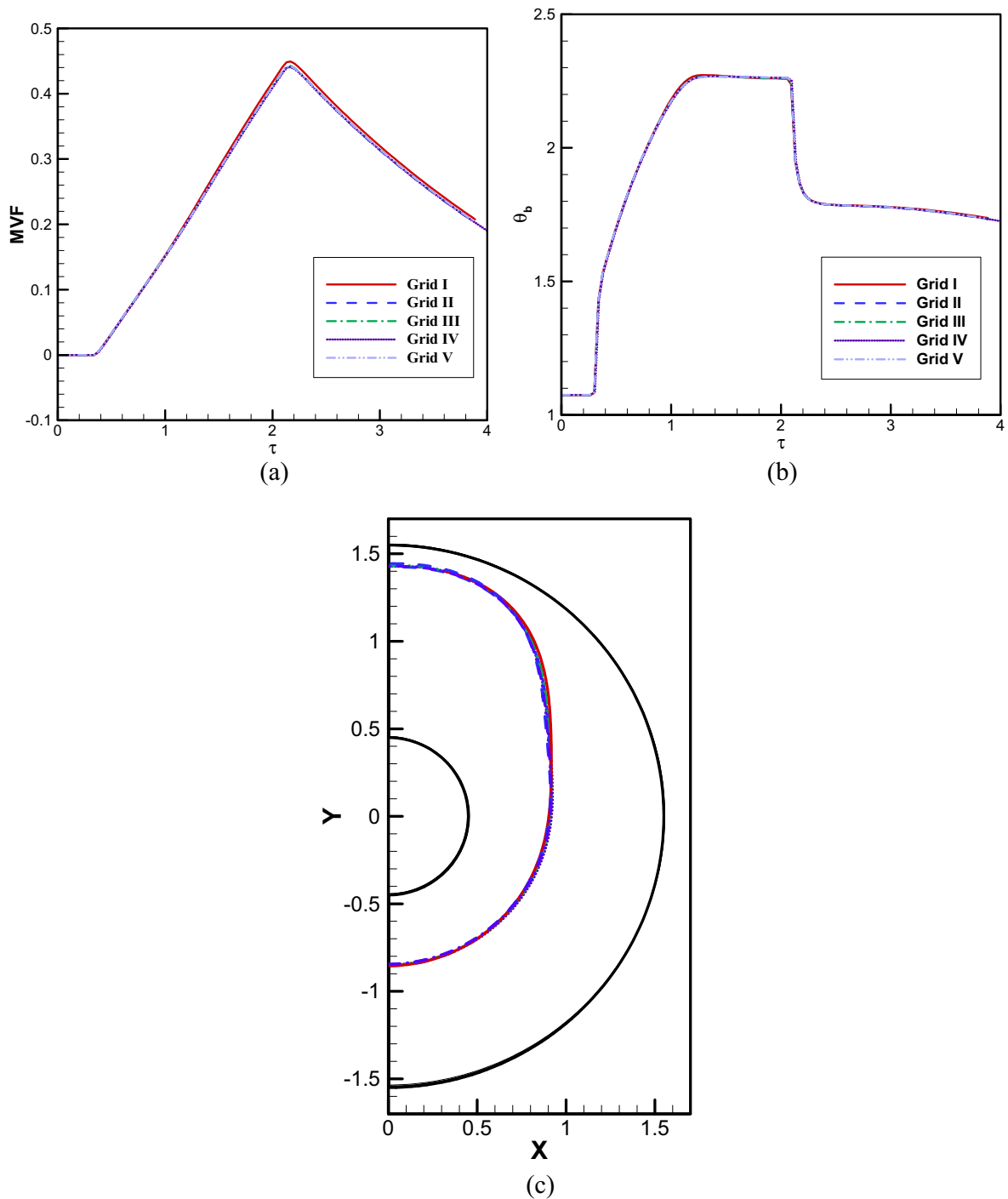
Fig. 2. The effect of grid size on: (a) the melt volume fraction (*MVF*); (b): the hot surface temperature ($\theta_{b,ave}$); (c): the melting interface at τ = 2.093.
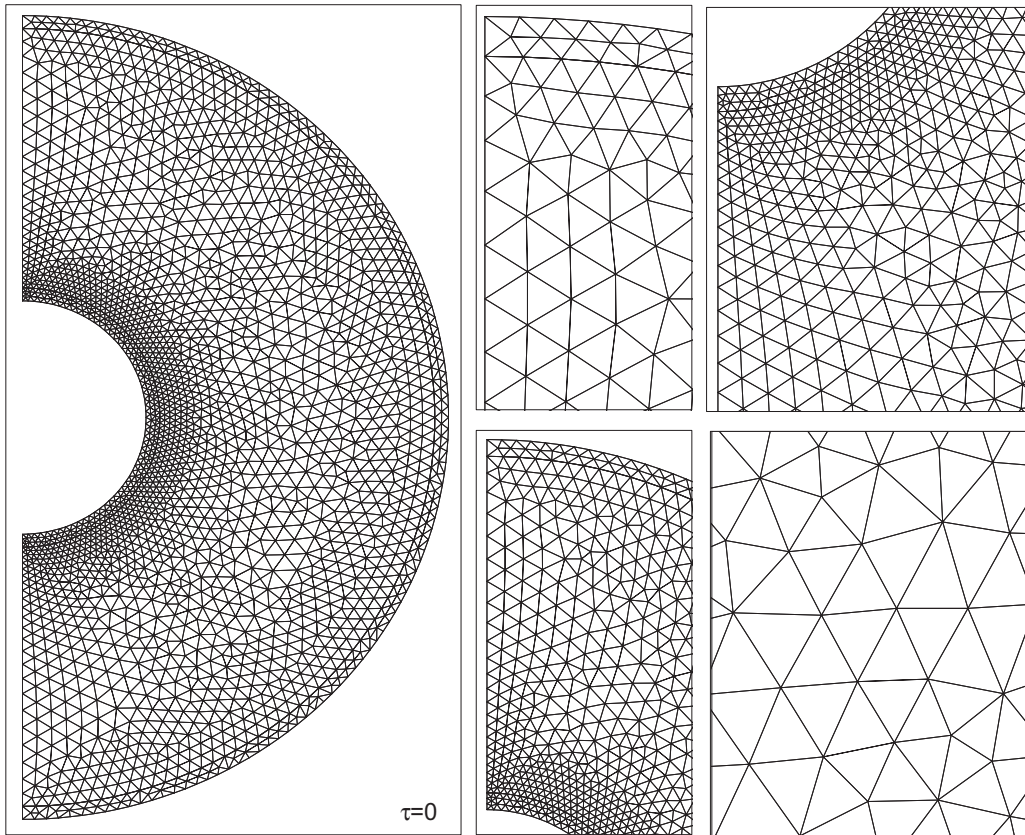
Fig. 3. A view of Grid IV, adopted for the computations of the present study.
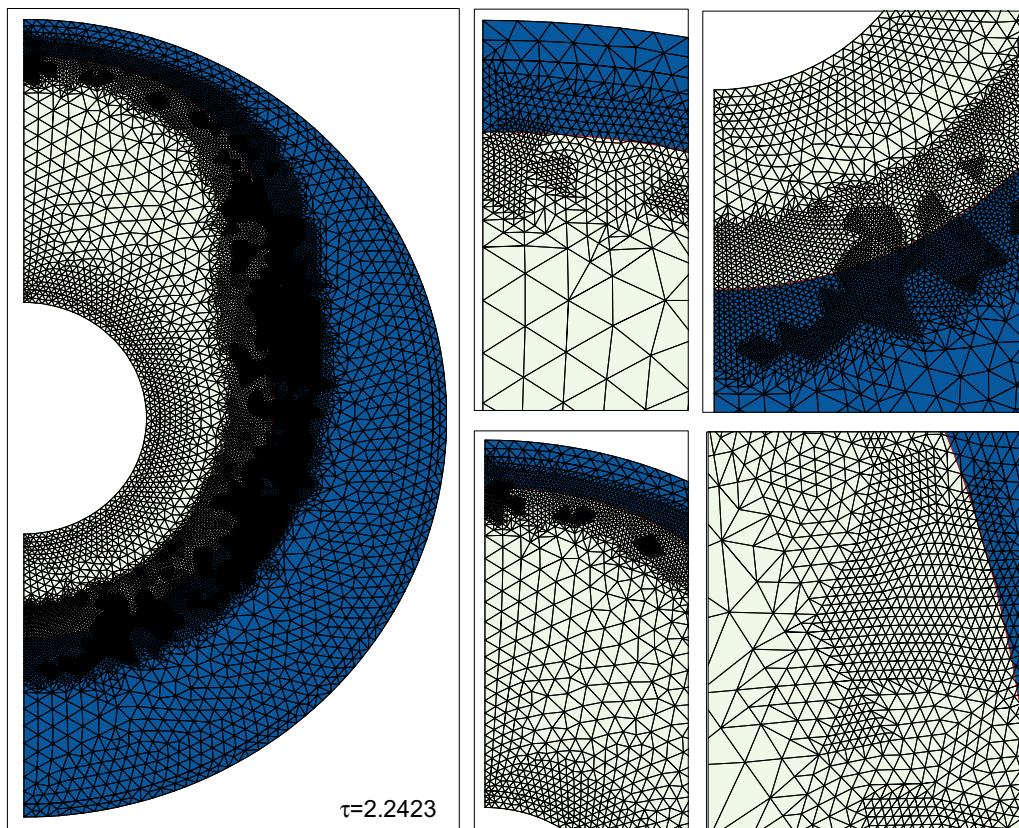
Fig. 4. A view of grid adaptation at $\tau = 2.093$; Light green is the liquid region, blue is the solid region, and the continues red line denotes the melting interface (ϕ=0.5). (For interpretation of the references to colour in this figure legend, the reader is referred to the web version of this article.)

(a): τ=0.37 (t=139s)   (b): τ=1.1 (t=416s)   (c): τ=1.47 (t=554s)
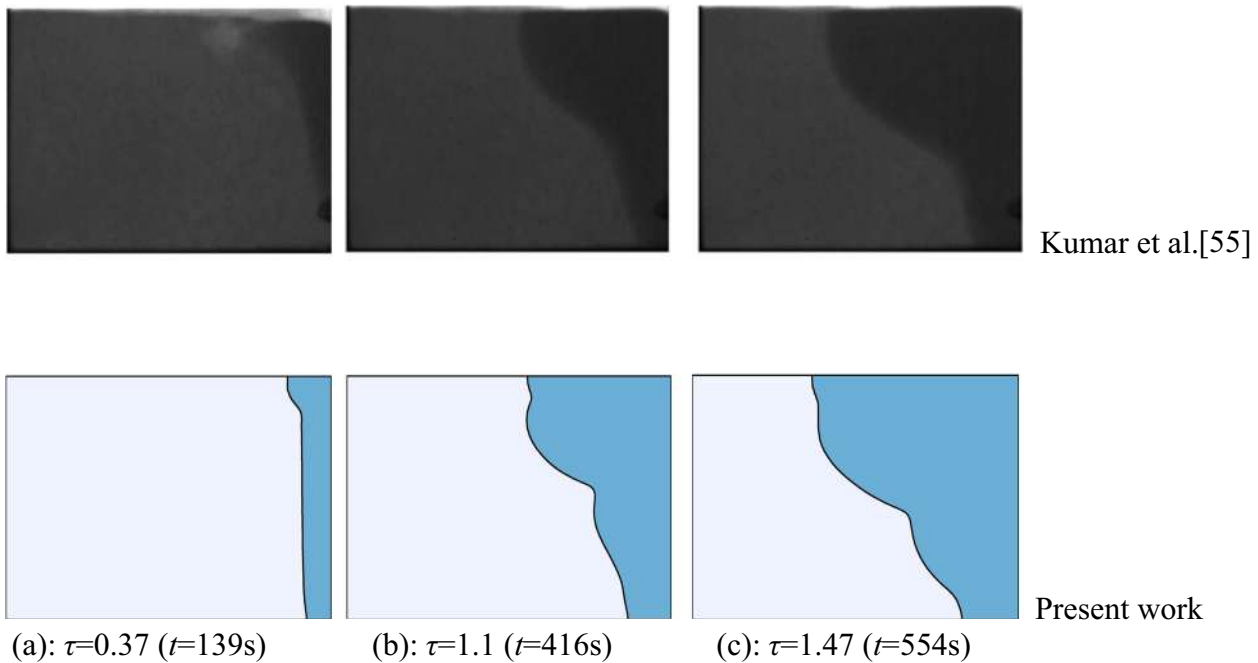
Fig. 5. A comparison between the melting interface reported in the experimental study of Kumar et al. [55] and the numerical results of the present work.
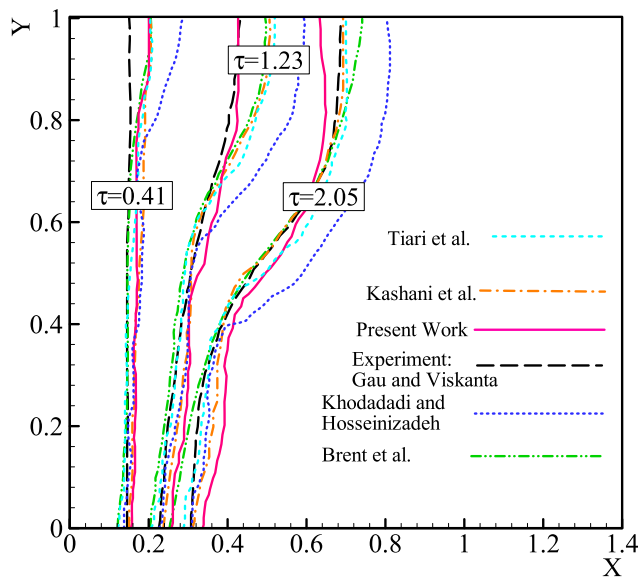
Fig. 6. A comparison between the melting interface reported in the experimental and numerical works in the literature [13,56–59] and the results obtained in the present study.

wax inside the pores was k_{eff} = 5 W/m K, and the effective latent heat of phase change was $h_{sf,m}$ = 132.5 (kJ/kg). The permeability adopted as 2.7×10^{-7} [47]. The thermophysical properties of copper and paraffin wax are available in the text, and Table 1. The results are depicted in Fig. 7.

5. Results and discussion

The results are reported in two parts. In the first part, the effect of the presence of the PCM on the heat transfer behavior of heatsink at the steady-state condition will be discussed. In the steady solution, there is no pulse, and surface heat flux is constant. In this case, the income heat from the hot surface is in balance with the dissipated heat at the cooled surface. The PCM can be in a fully solid state, partially liquid state or fully liquid state, depending on the cooling power at the outer surface and the power of surface heat flux.

In the second part of the results, the effect of a transient heat pulse on the melting and solidification of PCM in the porous medium will be discussed. The thermal behavior of the heatsink for controlling of the hot wall and melting volume fraction of PCM will be addressed. As the results are in non-dimensional form, the word of non-dimensional will be omitted in the following text.

Table 4
A comparison between the obtained average Nusselt number at the hot wall and the results available in the literature.

Authors	$Ra \times Da$			
	10	100	1000	10,000
Bejan [60]		4.200	15.800	50.8
Beckermann et al. [61]		3.113		48.9
Moya et al. [62]	1.065	2.801		
Baytas and Pop [63]	1.079	3.160	14.060	48.330
Sheremet and Pop [64]	1.071	3.104	13.839	49.253
Ghalambaz et al. [65]	1.080	3.111	13.642	48.561
Present study	1.079	3.111	13.73	50.78

Table 5
The thermos-physical properties of copper foam as a porous matrix and paraffin wax as phase change material [40].

Material	ρ (kg/m³)	k (W/m K)	c_p (J/kg K)	h_{sf} (J/kg)	μ (Pa s)	β (1/K)
Copper foam	8900	380	386	148,800	–	–
Paraffin	900	0.3	2300	–	0.00324	0.0005

Zheng et al. [40]

Present study

(a): τ =1.4782 (t=5400 s)   (b): τ=2.9564 (t=10800s)   (c): τ=4.4347 (t=16200s)
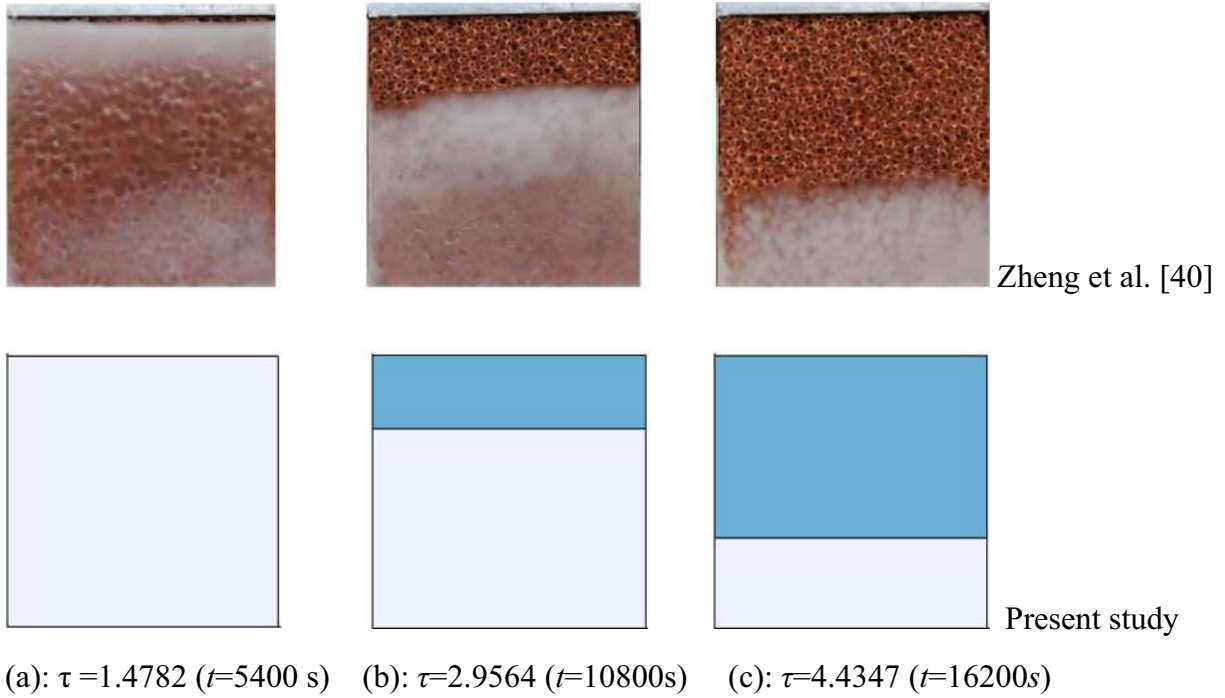
Fig. 7. A comparison between the experimental results of Zheng et al. [40] and numerical simulations in the present study.

(a)   (b)   (c)   (d)
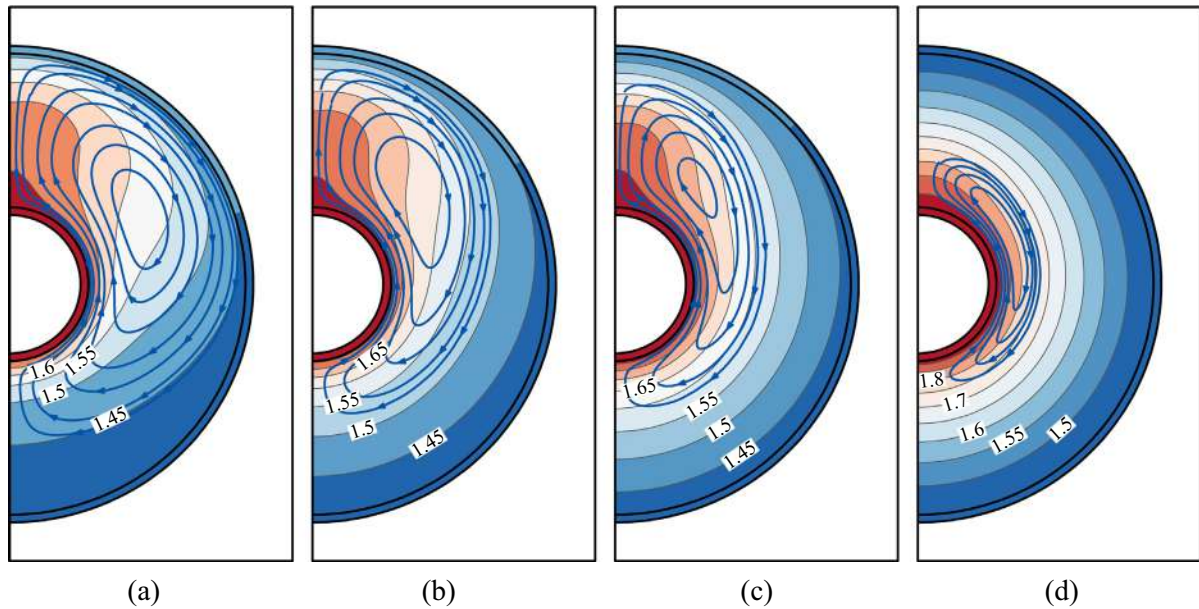
Fig. 8. The temperature distribution and streamlines when Bi = 0.2 and various values of non-dimensional fusion temperature (θ_f); (a): θ_f = 1.379 (MVF = 0.974 and $\theta_{b,ave}$ = 1.714); (b): θ_f = 1.446 (MVF = 0.838 and $\theta_{b,ave}$ = 1.767); (c): θ_f = 1.512 (MVF = 0.64 and $\theta_{b,ave}$ = 1.826); (d): θ_f = 1.646 (MVF = 0.351 and $\theta_{b,ave}$ = 1.931).
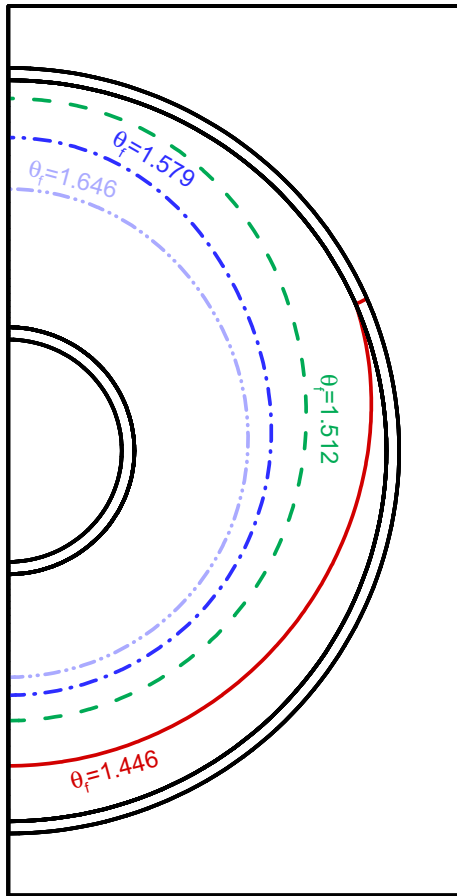
Fig. 9. The temperature distribution and streamlines when Bi = 0.2.

5.1. The steady state heat transfer (case $\gamma = 0$)

Fig. 8 illustrates the isotherms and streamlines for various values of fusion temperature, θ_f. The temperature level of $\theta = \theta_f$ can be considered as the melting interface. The values of normalized melt volume fraction and the temperature of the hot surface, $\theta_{b,ave}$, are also reported in the figure caption. As seen, by an increase of fusion temperature, the molten area reduces. For low values of fusion temperature, a large area of the heatsink is at the molten state. The molten state is developed toward the top areas of the heatsink due to the effect of natural convection heat transfer.

The temperature contours show a lower temperature at the hot surface in the case of low fusion temperature. Since the results are reported for a steady state case, the generated heat by the battery (hot surface) should be extracted at the cold surface. In the case of low fusion temperature, a large area of the heatsink is in a molten state, in which the natural convective heat transfer exists. Therefore, the thermal resistance between the hot surface and external cooling power is low, and consequently, the temperature difference between the hot surface and external flow is low. As the non-dimensional external temperature is fixed at zero, a low-temperature difference between the hot surface and external flow can be reflected in a low non-dimensional hot surface temperature. The situation is reversed in the case of high fusion temperature, in which a large portion of the heat sink area is in a solid state with a high thermal resistance (no natural convection). Hence, the temperature difference between the hot surface and the external flow will be high. The hot surface temperature for the case of θ_f = 1.379 is equal to $\theta_{b,ave}$ = 1.714, while for the case of θ_f = 1.646 is equal to $\theta_{b,ave}$ = 1.931. About 20% relative increase in θ_f from 1.379 to 1.646 results in about 12% relative increase in $\theta_{b,ave}$.

Fig. 9 depicts the location of the melting interface for various values of fusion temperature, θ_f. As seen, when the fusion temperature is low, the melting interface exists next to the cold wall. The increase of fusion temperature shifts the melting temperature toward the hot wall. When the fusion temperature is low, the melting interface is notably expanded toward the top areas of the heatsink. This is because the larger the molten area, the stronger natural convection flows.

Fig. 10 displays the normalized melt volume fraction (*MVF*) and the hot surface temperature, $\theta_{b,ave}$, as a function of external cooling power, Bi, for various values of fusion temperature. Fig. 11 depicts the same results but as a function of fusion temperature. For low values of Bi number, the normalized melting volume fraction is fixed at unity, which shows the entire of the heatsink is at the molten state. Indeed, the low Biot number indicates low external cooling power, and consequently, higher thermal resistance between the hot surface and cold external flow. Therefore, the temperature of PCM in
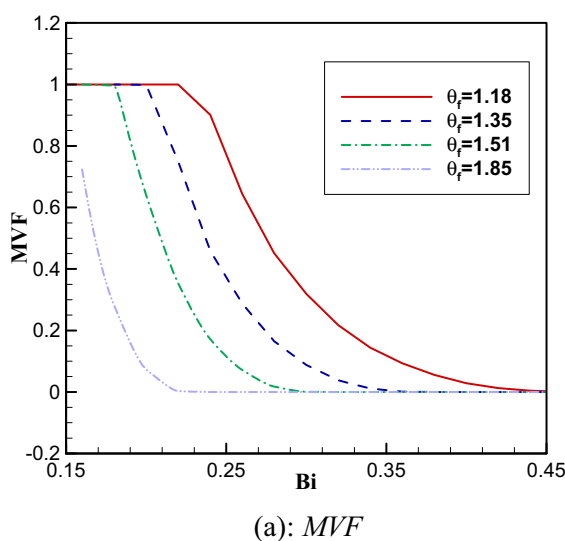
(a): *MVF*
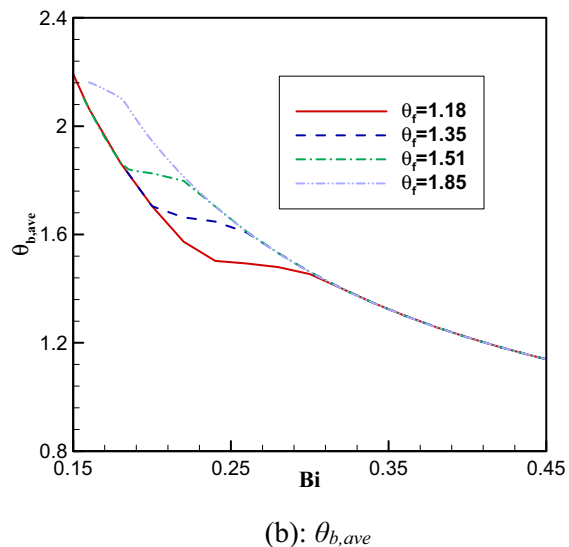
(b): $\theta_{b,ave}$

Fig. 10. The melt volume fraction (*MVF*) and non-dimensional hot wall temperature ($\theta_{b,ave}$) as a function of Biot number (*Bi*) for various values of the non-dimensional fusion temperature (θ_f).
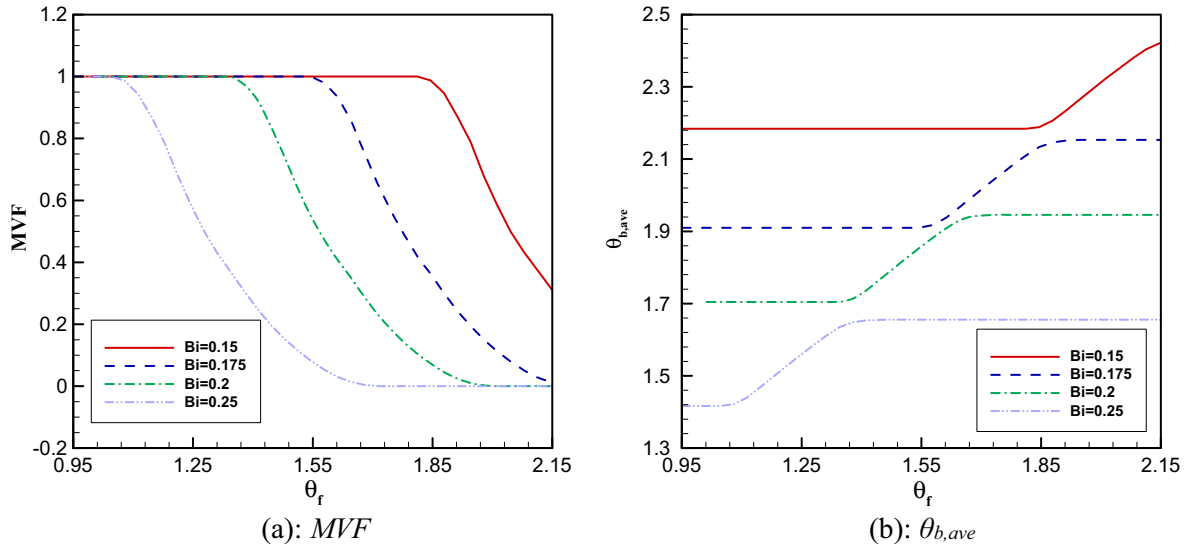
Fig. 11. The melt volume fraction (*MVF*) and non-dimensional hot wall temperature ($\theta_{b,ave}$) as a function of θ_f for various values of Biot number (*Bi*).

the heatsink will be higher than the fusion temperature. By the increase of Biot number, *MVF* reduces. Regardless of the fusion temperature, *MVF* is about zero for high values of Biot number as long as the non-dimensional fusion temperature is positive. It should be noted that a negative fusion temperature shows a fusion temperature lower than the external cooling temperature, and, no solidification can occur regardless of the magnitude of the Biot number. Hence, a negative fusion temperature has not been studied here.

The increase of Biot number also reduces the hot surface temperature almost linearly except for a region that the phase change occurs. For high values of Biot number, in which, the heatsink is in a fully solid-state, the influence of the variation of fusion temperature is negligible. However, for moderate values of Biot number, in which, the heatsink is in the two-phase state, the fusion temperature dictates the range of hot surface temperature. Interestingly, when the heatsink is in a two-phase state, the hot surface temperature is about the fusion temperature. Fig. 11 shows that the variation of fusion temperature almost induces the same effect as the variation of Biot number. Indeed, the external cooling power is the multiple of $Bi \times \theta_f$. However, the fusion temperature would

also affect the molten and solid areas of the heatsink in a non-linear way.

Fig. 12 shows the simultaneous effect of Biot number and fusion temperature on *MVF* and $\theta_{b,ave}$ in the form of contours. About 4000 cases were executed to plot the contours of Fig. 12(a and b). These contours illustrate a full map of the phase change behavior of the heatsink by the variation of *Bi* and θ_f. Fig. 12, in agreement with Figs. 10 and 11, confirm the existence of a liquid region for low values of *Bi* and fusion temperature in the heatsink. Interestingly, Fig. 12(a) shows that the difference between the fully melted region and fully solid region reduces by the increase of *Bi* and θ_f. In the two-phase state, the hot surface temperature is much sensitive to the fluctuation of the fusion temperature rather than the Biot number.

5.2. The unsteady heat pulse

Fig. 13 shows the isotherms and streamlines in the heatsink at various time sequences. The solution at time steps of $\tau = 0$ and $\tau = 0.299$ are steady state, and hence, the isotherms are identical.
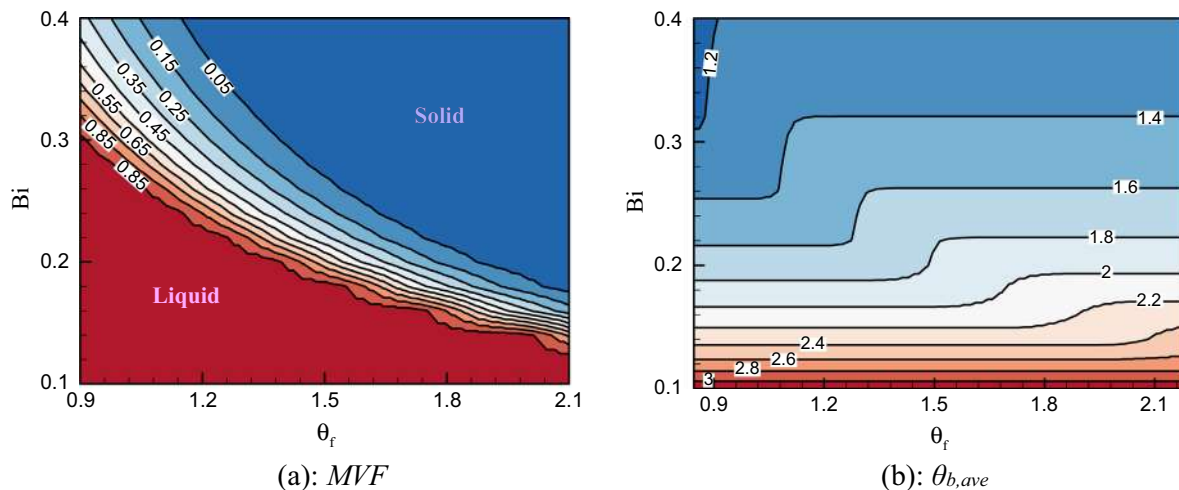
Fig. 12. The contours of melt volume fraction (*MVF*) and non-dimensional hot wall temperature ($\theta_{b,ave}$) as a function of non-dimensional fusion temperature (θ_f) and Biot number (*Bi*); (a): MVF and (b): Average hot wall temperature ($\theta_{b,ave}$).
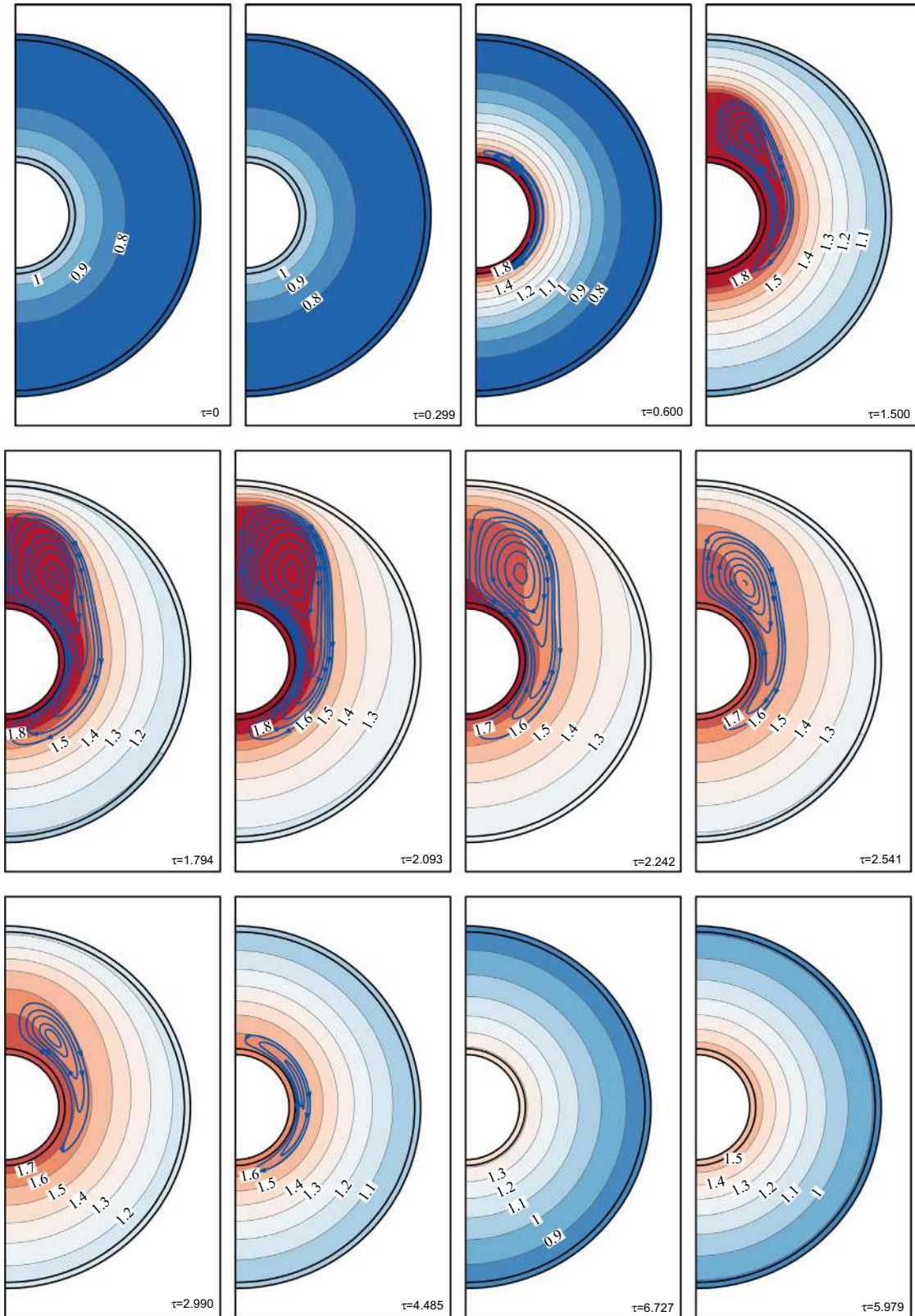
Fig. 13. The isotherms and streamlines during the melting and solidification of PCM subject to the pulse heat flux when θ_f = 1.512.

Moreover, the entire area of the heatsink is in a solid state, and thus, there is no streamline to report. The heat pulse with the power of γ = 3 is activated at τ = 0.299 and remains active until τ = 2.093. At τ = 0.6, the first molten area forms and streamlines

appear. In the time step of τ = 1.5, the molten region has advanced, and the convection flows at the top of the heatsink are notable. At τ = 1.794 and τ = 2.093, the melted area future expands but smoothly. The smooth expanse of the molten region is due to the

reduction in the thermal resistance between the hot surface and the external cooling flow by the increase of molten region and ease of convection heat transfer. At $\tau = 2.093$, the pulse load turns off ($\gamma = 0$). Hence, at $\tau = 2.242$, a contraction of the molten region can be observed compared to the case of $\tau = 2.093$. However, the temperature distribution is not the same as the case of $\tau = 1.794$ due to non-linearity of the convection heat transfer and transient effects. Time sequences of $\tau = 2.541$–6.727 illustrates the advancement of the solidification process. Although the melting process occurs during $\delta\tau = 1.794$, it took $\delta\tau = 4.634$ (about 2.5 times of the active pulse duration) to enclosure reaches a fully solid-state. The comparison between the isothermal of the steady-state solution, at the initial time of $\tau = 0$ and the final time of $\tau = 6.727$, shows that the heatsink has not reached a fully steady-state condition yet.

Fig. 14 depicts the variation of characteristic parameters of hot surface temperature ($\theta_{b,ave}$), normalized melt volume fraction (MVF) and heatsink efficiency (η) as a function of non-dimensional time (τ) for various values of fusion temperature. Fig. 15 displays the same results for various values of the Biot number. Using the temperature map of Fig. 12, in the case of the defult value of Bi = 0.5 and a fusing temperature about $\theta_f = 1.5$, the heat sink is uniformly at a solid-state. Hence, considering Fig. 14, at the initial time, in which the pulse load is not activated yet, the effect of fusion temperature is negligible since the heatsink is in a fully solid-state and $MVF = 0$. At this stage, η is about 1.8. This efficiency is due to the increased surface of the outer cylinder compared to the battery shield. By the activation of pulse load, the molten volume fraction grows sharply, and the hot surface temperature ($\theta_{b,ave}$) is also raised. The increase in the temperature of the hot surface is due to the increased power of the heat load. During $\tau = 1$ to $\tau = 2$, the hot surface experience a constant temperature. At the initial stage of phase change, in which the PCM in the heatsink is in a fully solid state, the thermal resistance of PCM due to pure conduction is high. Hence, the temperature of the hot surface raises gradually. After a while, in which the molten region expands, and natural convection effects dominate the heat transfer, the temperature of the hot surface is controlled by the fusion temperature at a constant temperature.

(a)

(b)

(c)
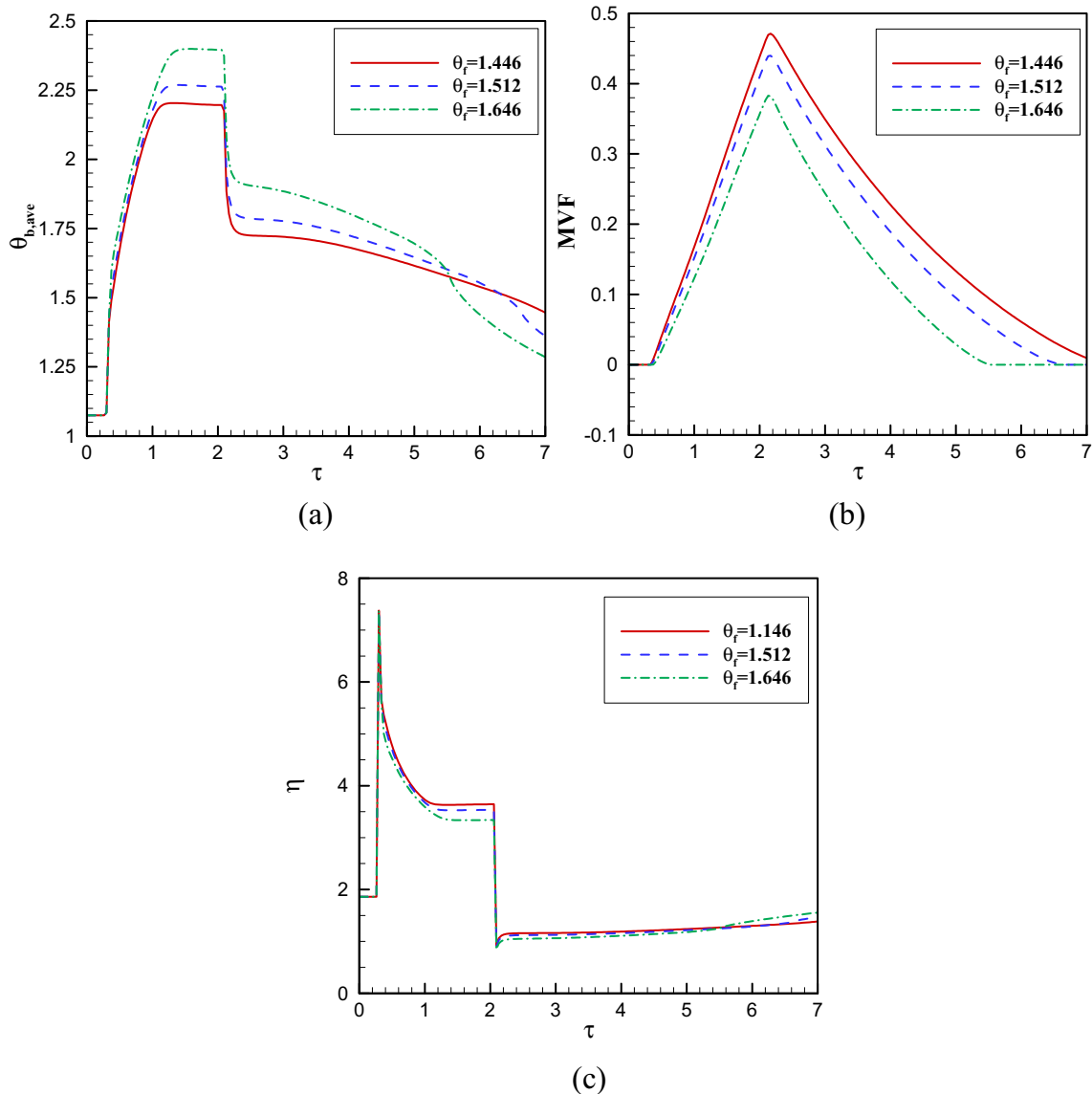
Fig. 14. The variation of characteristic parameters during the heat pulse and after the heat pulse for various values of non-dimensional fusion temperature (θ_f); (a): the non-dimensional hot wall temperature ($\theta_{b,ave}$); (b): melting volume fraction; (c): cooling efficiency of using PCMs (η).
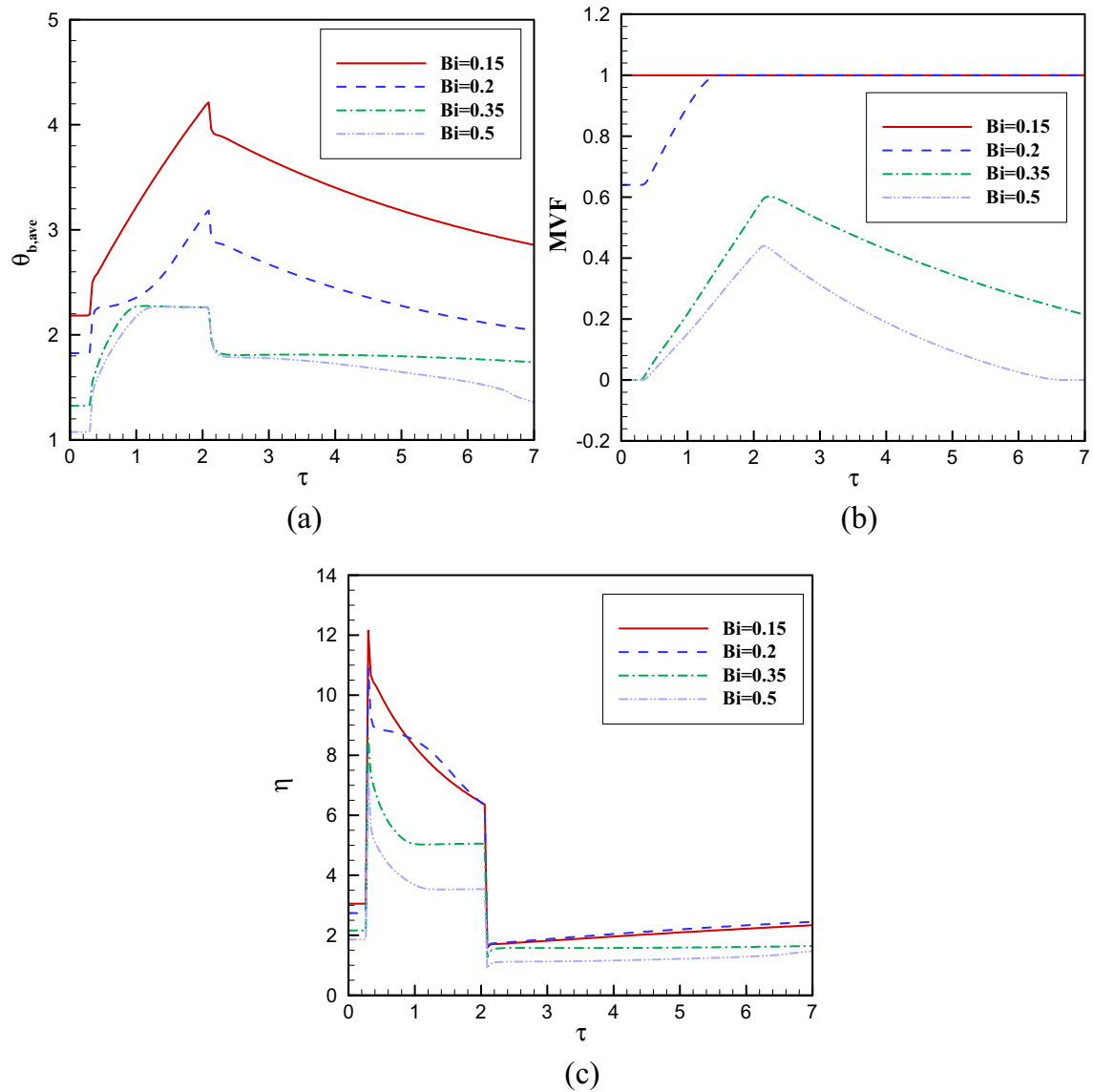
Fig. 15. The variation of characteristic parameters during the heat pulse and after the heat pulse for various values of Biot number (*Bi*) at the outer surface of the cavity; (a): the non-dimensional hot wall temperature ($\theta_{b,ave}$); (b): melting volume fraction; (c): cooling efficiency (η) of using PCMs.

At the end of pulse load, the temperature of hot surface drops instantly, due to the substantial convection heat transfer in the molten region of the heatsink. After that, the hot surface temperature drops smoothly in the solidification process. A non-linear behavior for $\theta_{b,ave}$ can be observed at the end of the solidification process. This non-linear behavior commences when the PCM reaches into a fully solid state, and consequently, the latent heat storage changes to the sensible heat storage.

The heatsink efficiently experiences a drastic increase, up to $\eta = 7.5$, when the pulse heat flux jumps to $1 + \xi$. This pick efficiency is due to the vicinity of the cold PCM and the hot surface. Then, heatsink efficiently drops sharply as the melting region advances by pure conduction. During this state, the thermal resistance due to pure conduction in PCM-metal foam around the hot surface is very high and increases by the advancement of the melting surface away from the hot surface. After this stage, the natural convection flows in the molten region take place, and the heatsink efficiency remains constant about $\eta = 4$. Then, the pulse load turns off, and the heat sink efficiency instantly drops to about unity, and smoothly raises during the solidification process. The variation of fusion temperature shifts this behavior but does not change the

trend of the results. Hence, the fusion temperature is an essential parameter for the heatsink design. The fusion temperature particularly influences the hot surface temperature without affecting the general behavior of the heatsink.

Moreover, when the fusion temperature is minimal the melt volume fraction is maximum regardless of the time history. Indeed, the heat of the heat flux at the hot wall is absorbed by the porous matrix and the PCM inside the pores in the form of sensible heat and the latent heat. A higher fusion temperature results in a larger sensible heat before the fusion occurs. Thus, as a larger portion of the energy of the hot wall is absorbed by sensible heat of the heat sink a lower portion of latent heat and melt volume fraction can be expected. Hence, as seen in Fig. 14(a) the higher the fusion temperature, the lower the *MVF*.

Fig. 15 reveals that the increase of Biot number decreases the hot surface temperature and *MVF* by boosting the cooling power at the external surface of the heatsink. Generally, the efficiency of the heatsink is higher at lower Biot numbers. Therefore, using phase change heatsink is of interest in situations with low external convection or spaces with low ventilation. The case of *Bi* = 0.15 in Fig. 15(b) is a straight line. Attention to Fig. 12 shows that in the

case of θ_f = 1.512 and Bi = 0.15, the entire cavity heat sink is in the molten phase at the steady-state. Hence, increasing heat flux (during the pulse) increases the superheat degree of the molten PCM and does not contribute to the increase of MVF. Moreover, in the case of Bi = 0.2, most of the heat sink is initially (steady-state situation) at the molten phase. Hence, increasing the heat flux during the heat pulse melts the small fraction of solid quickly, and MVF reaches unity and remains the same.

6. Conclusion

The phase change heat transfer in a phase change heatsink consisted of two horizontal cylinders filled with a metal foam saturated by a phase change material was theoretically studied. The cooling performance of the heatsink and the energy storage/release due to an unsteady pulse load were investigated. The finite element method, along with a grid adaptation and automatic time stepping control, was employed to solve the governing equations. The results were reported for various values of non-dimensional fusion temperature and Biot number in both cases of steady equilibrium solution and unsteady heat pulse. The main outcomes of the study can be summarized as follows:

1. The increase of fusion temperature or Biot number reduces the overall melt fraction in the heatsink at steady state conditions in the absence of a pulse load. This means the higher fusion temperature or external cooling power the cooling energy can be stored in the heatsink.
2. During the pulse load, the increase of the fusion temperature slightly reduces the heatsink cooling efficiency. Regardless of the fusion temperature, the cooling efficiency of the phase change heatsink is higher than unity.
3. During the pulse load, the lower the external cooling power (the lower the Biot number), the higher the heatsink efficiency. The efficiency of heatsink during the pulse load increases from $\eta \sim 4$ to $\eta \sim 5$ by the reduction of Biot number from Bi = 0.5 to Bi = 0.35.
4. The solidification time is about 2.5 times higher than the melting time. This is since the natural convection flow aids the melting process.

In the present study, the influence of fusion temperature and external cooling power (Biot number) on the thermal performance of a PCM-metal foam heatsink were addressed. The results show that the melting was firstly extended at the top areas of heatsink due to the natural convection effects. Therefore, the contribution of bottom areas of heatsink on the heat transfer was small. Some eccentricity of the hot surface may help with a better heat transfer. Moreover, a non-uniform distribution of metal foam, in the form of a heatsink partially filled with metal foam, may also enhance the heatsink efficiency, which can be subject of future studies.

Declaration of Competing Interest

The authors clarify that there is no conflict of interest for report.

Acknowledgement

References

[1] M. Chen, Y. He, Q. Ye, Z. Zhang, Y. Hu, Solar thermal conversion and thermal energy storage of CuO/Paraffin phase change composites, Int. J. Heat Mass Transf. 130 (2019) 1133–1140.
[2] M. Ismail, Application of phase change materials (PCMs) in building walls: a review, Adv. Civil Eng. Mater. (2019) 73.
[3] H. Panchal, J. Patel, S. Chaudhary, A comprehensive review of solar cooker with sensible and latent heat storage materials, Int. J. Ambient Energy 40 (3) (2019) 329–334.
[4] R.O. Lamidi, L. Jiang, P.B. Pathare, Y. Wang, A. Roskilly, Recent advances in sustainable drying of agricultural produce: a review, Appl. Energy 233 (2019) 367–385.
[5] L. Mishra, A. Sinha, R. Gupta, Recent Developments in Latent Heat Energy Storage Systems Using Phase Change Materials (PCMs)—A Review, in: Green Buildings and Sustainable Engineering, Springer, 2019, pp. 25–37.
[6] R. Baby, C. Balaji, Thermal Management of Electronics, Phase Change Material-Based Composite Heat Sinks—An Experimental Approach, Momentum Press, 2019.
[7] J.T. Evans, A.C. Wood, C.E. Boyack, R. Piekarski, Phase change material heat sink using additive manufacturing and method, Google Patents (2019).
[8] M. Sheikholeslami, M. Jafaryar, A. Shafee, Z. Li, Hydrothermal and second law behavior for charging of NEPCM in a two dimensional thermal storage unit, Chin. J. Phys. 58 (2019) 244–252.
[9] M. Sheikholeslami, R.-U. Haq, A. Shafee, Z. Li, Heat transfer behavior of nanoparticle enhanced PCM solidification through an enclosure with V shaped fins, Int. J. Heat Mass Transf. 130 (2019) 1322–1342.
[10] Z. Li, M. Sheikholeslami, A. Shafee, R.-U. Haq, I. Khan, I. Tlili, R. Kandasamy, Solidification process through a solar energy storage enclosure using various sizes of Al2O3 nanoparticles, J. Mol. Liq. 275 (2019) 941–954.
[11] M.Y. Yazici, M. Avci, O. Aydin, Combined effects of inclination angle and fin number on thermal performance of a PCM-based heat sink, Appl. Therm. Eng. 113956 (2019).
[12] R. Kalbasi, M. Afrand, J. Alsarraf, M.-D. Tran, Studies on optimum fins number in PCM-based heat sinks, Energy 171 (2019) 1088–1099.
[13] S. Tiari, S. Qiu, M. Mahdavi, Numerical study of finned heat pipe-assisted latent heat thermal energy storage system, APS Meeting Abstracts, 2014.
[14] S. Tiari, O.L. Rose, M. Mahdavi, Discharging Process of a High-Temperature Heat Pipe-assisted Thermal Energy Storage System with Nano-enahnced Phase Change Material, ASTFE Digital Library, Begel House Inc., 2019.
[15] A. Pourakabar, A.A.R. Darzi, Enhancement of phase change rate of PCM in cylindrical thermal energy storage, Appl. Therm. Eng. 150 (2019) 132–142.
[16] L. Zhang, K. Zhou, Q. Wei, L. Ma, W. Ye, H. Li, B. Zhou, Z. Yu, C.-T. Lin, J. Luo, Thermal conductivity enhancement of phase change materials with 3D porous diamond foam for thermal energy storage, Appl. Energy 233 (2019) 208–219.
[17] T.-U. Rehman, H.M. Ali, M.M. Janjua, U. Sajjad, W.-M. Yan, A critical review on heat transfer augmentation of phase change materials embedded with porous materials/foams, Int. J. Heat Mass Transf. 135 (2019) 649–673.
[18] N.S. Bondareva, M.A. Sheremet, Flow and heat transfer evolution of PCM due to natural convection melting in a square cavity with a local heater, Int. J. Mech. Sci. 134 (2017) 610–619.
[19] N.S. Bondareva, M.A. Sheremet, Conjugate heat transfer in the PCM-based heat storage system with finned copper profile: application in electronics cooling, Int. J. Heat Mass Transf. 124 (2018) 1275–1284.
[20] N.S. Bondareva, B. Buonomo, O. Manca, M.A. Sheremet, Heat transfer inside cooling system based on phase change material with alumina nanoparticles, Appl. Therm. Eng. 144 (2018) 972–981.
[21] F. Iachachene, Z. Haddad, H.F. Oztop, E. Abu-Nada, Melting of phase change materials in a trapezoidal cavity: orientation and nanoparticles effects, J. Mol. Liq. (2019).
[22] M. Ghalambaz, A. Doostani, E. Izadpanahi, A.J. Chamkha, Phase-change heat transfer in a cavity heated from below: the effect of utilizing single or hybrid nanoparticles as additives, J. Taiwan Inst. Chem. Eng. 72 (2019) 104–115.
[23] M. Ghalambaz, A. Doostani, A.J. Chamkha, M.A. Ismael, Melting of nanoparticles-enhanced phase-change materials in an enclosure: effect of hybrid nanoparticles, Int. J. Mech. Sci. 134 (2017) 85–97.
[24] A. Doostani, M. Ghalambaz, A.J. Chamkha, MHD natural convection phase-change heat transfer in a cavity: analysis of the magnetic field effect, J. Braz. Soc. Mech. Sci. Eng. 39 (7) (2017) 2831–2846.
[25] S. Sivasankaran, A. Alsabery, I. Hashim, Internal heat generation effect on transient natural convection in a nanofluid-saturated local thermal non-equilibrium porous inclined cavity, Physica A 509 (2018) 275–293.
[26] A.I. Alsabery, T. Tayebi, A.J. Chamkha, I. Hashim, Effect of rotating solid cylinder on entropy generation and convective heat transfer in a wavy porous cavity heated from below, Int. Commun. Heat Mass Transf. 95 (2018) 197–209.
[27] A. Chamkha, F. Selimefendigil, MHD free convection and entropy generation in a corrugated cavity filled with a porous medium saturated with nanofluids, Entropy 20 (11) (2018) 846.
[28] A.J. Chamkha, I.V. Miroshnichenko, M.A. Sheremet, Unsteady conjugate natural convective heat transfer and entropy generation in a porous semicircular cavity, J. Heat Transf. 140 (6) (2018) 062501.
[29] A.F. Al-Mudhaf, A. Rashad, S.E. Ahmed, A.J. Chamkha, S. El-Kabeir, Soret and Dufour effects on unsteady double diffusive natural convection in porous trapezoidal enclosures, Int. J. Mech. Sci. 140 (2018) 172–178.

[30] M. Rajarathinam, N. Nithyadevi, A.J. Chamkha, Heat transfer enhancement of mixed convection in an inclined porous cavity using Cu-water nanofluid, Adv. Powder Technol. 29 (3) (2018) 590–605.

[31] Z. Li, A. Shafee, M. Ramzan, H. Rokni, Q.M. Al-Mdallal, Simulation of natural convection of Fe3O4-water ferrofluid in a circular porous cavity in the presence of a magnetic field, Eur. Phys. J. Plus 134 (2) (2019) 77.

[32] A. Andreozzi, N. Bianco, O. Manca, V. Naso, Numerical analysis of radiation effects in a metallic foam by means of the radiative conductivity model, Appl. Therm. Eng. 49 (2012) 14–21.

[33] X. Chen, X.-L. Xia, C. Sun, X.-W. Yan, Transient thermal analysis of the coupled radiative and convective heat transfer in a porous filled tube exchanger at high temperatures, Int. J. Heat Mass Transf. 108 (2017) 2472–2480.

[34] A. Andreozzi, N. Bianco, M. Iasiello, V. Naso, Numerical study of metal foam heat sinks under uniform impinging flow, J. Phys.: Conf. Ser., IOP Publish. (2017) 012002.

[35] X. Xiao, P. Zhang, M. Li, Preparation and thermal characterization of paraffin/metal foam composite phase change material, Appl. Energy 112 (2013) 1357–1366.

[36] M. Sheikholeslami, Solidification of NEPCM under the effect of magnetic field in a porous thermal energy storage enclosure using CuO nanoparticles, J. Mol. Liq. 263 (2018) 303–315.

[37] M. Sheikholeslami, Z. Li, A. Shafee, Lorentz forces effect on NEPCM heat transfer during solidification in a porous energy storage system, Int. J. Heat Mass Transf. 127 (2018) 665–674.

[38] Y. Xu, Q. Ren, Z.-J. Zheng, Y.-L. He, Evaluation and optimization of melting performance for a latent heat thermal energy storage unit partially filled with porous media, Appl. Energy 193 (2017) 84–95.

[39] M.T. Kohyani, B. Ghasemi, A. Raisi, S. Aminossadati, Melting of cyclohexane–Cu nano-phase change material (nano-PCM) in porous medium under magnetic field, J. Taiwan Inst. Chem. Eng. 77 (2017) 142–151.

[40] H. Zheng, C. Wang, Q. Liu, Z. Tian, X. Fan, Thermal performance of copper foam/paraffin composite phase change material, Energy Convers. Manage. 157 (2018) 372–381.

[41] P. Di Giorgio, M. Iasiello, A. Viglione, M. Mameli, S. Filippeschi, P. Di Marco, A. Andreozzi, N. Bianco, Numerical analysis of a paraffin/metal foam composite for thermal storage, J. Phys.: Conf. Ser., IOP Publish. (2017) 012032.

[42] S. Mancin, A. Diani, L. Doretti, K. Hooman, L. Rossetto, Experimental analysis of phase change phenomenon of paraffin waxes embedded in copper foams, Int. J. Therm. Sci. 90 (2015) 79–89.

[43] A. Hussain, C. Tso, C.Y. Chao, Experimental investigation of a passive thermal management system for high-powered lithium ion batteries using nickel foam-paraffin composite, Energy 115 (2016) 209–218.

[44] D.A. Nield, A. Bejan, Convection in Porous Media, Springer Science & Business Media, 2006.

[45] J. Buongiorno, Convective transport in nanofluids, J. Heat Transf. 128 (3) (2006) 240–250.

[46] M. Sheikholeslami, M. Shamlooei, R. Moradi, Fe3O4-Ethylene glycol nanofluid forced convection inside a porous enclosure in existence of Coulomb force, J. Mol. Liq. 249 (2018) 429–437.

[47] A. Bhattacharya, V. Calmidi, R. Mahajan, Thermophysical properties of high porosity metal foams, Int. J. Heat Mass Transf. 45 (5) (2002) 1017–1031.

[48] Engineersedge, Specific heat capacity of metals table chart, in.

[49] J.N. Reddy, An introduction to the finite element method, New York, 1993.

[50] J.N. Reddy, D.K. Gartling, The Finite Element Method in Heat Transfer and Fluid Dynamics, CRC Press, 2010.

[51] O.C. Zienkiewicz, R.L. Taylor, P. Nithiarasu, The Finite Element Method for Fluid Dynamics, The Finite Element Method for Fluid Dynamics, 7th ed., ButterworthHeinemann, Oxford, 2014.

[52] J.C. De Los Reyes, S. González Andrade, A combined BDF-semismooth Newton approach for time-dependent Bingham flow, Numer. Methods Partial Differ. Eq. 28 (3) (2012) 834–860.

[53] O. Schenk, K. Gärtner, Solving unsymmetric sparse systems of linear equations with PARDISO, Future Gener. Comput. Syst. 20 (3) (2004) 475–487.

[54] P. Wriggers, Nonlinear Finite Element Methods, Springer Science & Business Media, 2008.

[55] L. Kumar, B. Manjunath, R. Patel, S. Markandeya, R. Agrawal, A. Agrawal, Y. Kashyap, P. Sarkar, A. Sinha, K. Iyer, Experimental investigations on melting of lead in a cuboid with constant heat flux boundary condition using thermal neutron radiography, Int. J. Therm. Sci. 61 (2012) 15–27.

[56] C. Gau, R. Viskanta, Melting and solidification of a pure metal on a vertical wall, J. Heat Transf. 108 (1) (1986) 174–181.

[57] J. Khodadadi, S. Hosseinizadeh, Nanoparticle-enhanced phase change materials (NEPCM) with great potential for improved thermal energy storage, Int. Commun. Heat Mass Transf. 34 (5) (2007) 534–543.

[58] S. Kashani, A. Ranjbar, M. Abdollahzadeh, S. Sebti, Solidification of nano-enhanced phase change material (NEPCM) in a wavy cavity, Heat Mass Transf. 48 (7) (2012) 1155–1166.

[59] A. Brent, V.R. Voller, K. Reid, Enthalpy-porosity technique for modeling convection-diffusion phase change: application to the melting of a pure metal, Numer. Heat Transf., Part A Appl. 13 (3) (1988) 297–318.

[60] A. Bejan, On the boundary layer regime in a vertical enclosure filled with a porous medium, Lett. Heat Mass Transf. 6 (2) (1979) 93–102.

[61] C. Beckermann, R. Viskanta, S. Ramadhyani, A numerical study of non-Darcian natural convection in a vertical enclosure filled with a porous medium, Numer. Heat Transf. 10 (6) (1986) 557–570.

[62] S.L. Moya, E. Ramos, M. Sen, Numerical study of natural convection in a tilted rectangular porous material, Int. J. Heat Mass Transf. 30 (4) (1987) 741–756.

[63] A.C. Baytas, I. Pop, Free convection in oblique enclosures filled with a porous medium, Int. J. Heat Mass Transf. 42 (6) (1999) 1047–1057.

[64] M.A. Sheremet, I. Pop, Natural convection in a square porous cavity with sinusoidal temperature distributions on both side walls filled with a nanofluid: Buongiorno's mathematical model, Transp. Porous Media 105 (2) (2014) 411–429.

[65] M. Ghalambaz, H. Hendizadeh, H. Zargartalebi, I. Pop, Free convection in a square cavity filled with a tridisperse porous medium, Transp. Porous Media 116 (1) (2017) 379–392.